Article

Cell

Chromothripsis and Kataegis Induced by Telomere Crisis

Graphical Abstract

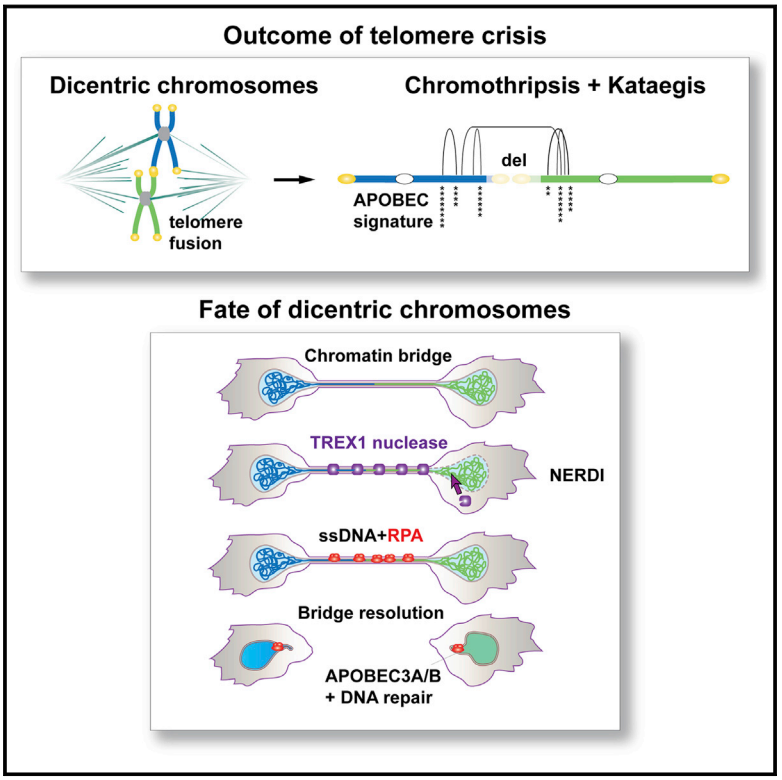

Highlights

- Dicentric chromosomes formed during telomere crisis do not break in mitosis
- Cells with dicentrics develop chromatin bridges that induce nuclear envelope rupture
- The TREX1 3′ nuclease generates ssDNA in the bridges and facilitates their resolution
- Post-telomere crisis cells often show chromothripsis and kataegis

Authors

John Maciejowski, Yilong Li, Nazario Bosco, Peter J. Campbell, Titia de Lange

Correspondence

delange@mail.rockefeller.edu (T.d.L.), pc8@sanger.ac.uk (P.J.C.)

In Brief

During telomere crisis, dicentric chromosomes form long chromatin bridges that induce nuclear envelope rupture. Nucleolytic attack of the dicentric chromosomes generates extensive ssDNA and leads to bridge breakage, which may contribute to the occurrence of chromothripsis and kataegis in cancer genomes.

Maciejowski et al., 2015, Cell *163*, 1641–1654
December 17, 2015
http://dx.doi.org/10.1016/j.cell.2015.11.054

CellPress

Cell

Chromothripsis and Kataegis Induced by Telomere Crisis

John Maciejowski,[1] Yilong Li,[2] Nazario Bosco,[1] Peter J. Campbell,[2,*] and Titia de Lange[1,*]
[1]Laboratory for Cell Biology and Genetics, The Rockefeller University, 1230 York Avenue, New York, NY 10065, USA
[2]Wellcome Trust Sanger Institute, Wellcome Trust Genome Campus, Hinxton Cambridge, CB10 1SA, UK
*Correspondence: delange@mail.rockefeller.edu (T.d.L.), pc8@sanger.ac.uk (P.J.C.)
http://dx.doi.org/10.1016/j.cell.2015.11.054

SUMMARY

Telomere crisis occurs during tumorigenesis when depletion of the telomere reserve leads to frequent telomere fusions. The resulting dicentric chromosomes have been proposed to drive genome instability. Here, we examine the fate of dicentric human chromosomes in telomere crisis. We observed that dicentric chromosomes invariably persisted through mitosis and developed into 50–200 μm chromatin bridges connecting the daughter cells. Before their resolution at 3–20 hr after anaphase, the chromatin bridges induced nuclear envelope rupture in interphase, accumulated the cytoplasmic 3′ nuclease TREX1, and developed RPA-coated single stranded (ss) DNA. CRISPR knockouts showed that TREX1 contributed to the generation of the ssDNA and the resolution of the chromatin bridges. Post-crisis clones showed chromothripsis and kataegis, presumably resulting from DNA repair and APOBEC editing of the fragmented chromatin bridge DNA. We propose that chromothripsis in human cancer may arise through TREX1-mediated fragmentation of dicentric chromosomes formed in telomere crisis.

INTRODUCTION

The view that dicentric chromosomes are broken in mitosis and undergo breakage-fusion-bridge (BFB) cycles originates from McClintock's cytological observation of corn chromosomes (McClintock, 1938; McClintock, 1941). More recently, the fate of dicentric chromosomes has been studied in yeast as well as plants (reviewed in Stimpson et al., 2012). Here, we document the behavior of dicentric chromosomes in human cells.

Dicentric chromosomes can be formed during the early stages of human tumorigenesis when telomere shortening has led to dysfunctional telomeres (reviewed in Artandi and DePinho, 2010). Telomere shortening induces senescence or apoptosis when a few telomeres lose the ability to repress DNA damage signaling pathways. Telomere fusions are infrequent in senescence, most likely because of the low frequency of dysfunctional telomeres. Upon by-pass of senescence due to loss of p53 and Rb, further telomere attrition increases the incidence of telomere dysfunction, eventually leading to a telomere crisis where telomeres fuse to form dicentric chromosomes. These dicentrics have been proposed to drive genome instability in cancer. The genomic scars indicative of past telomere crisis have been observed in several types of cancer (Lin et al., 2010; Lin et al., 2014; Roger et al., 2013; Simpson et al., 2015). However, the fate of dicentric chromosomes, including potential BFB cycles, has been elusive.

The genomic footprint of BFB cycles is a "fold-back" inverted rearrangement that demarcates a region of amplification from a terminal chromosomal deletion. Such events have been observed in pancreatic cancer, esophageal cancer, breast cancer, and leukemias, among others (Bignell et al., 2007; Campbell et al., 2010; Waddell et al., 2015; Li et al., 2014; Nones et al., 2014). Interestingly, several of these studies have suggested an association between the rearrangements of BFB cycles and chromothripsis (Nones et al., 2014; Li et al., 2014). Chromothripsis is a mysterious mutational process in which one or more localized chromosomal regions undergo catastrophic shattering, triggering a haphazard repair process of stitching chromosomal fragments together in a random order and orientation (Stephens et al., 2011). Chromothripsis has been observed across many tumor types (Forment et al., 2012), especially those with p53 loss (Rausch et al., 2012), as well as occasional occurrence in the germline (Kloosterman and Cuppen, 2013). Chromothripsis breakpoints often show clusters of base substitutions localized nearby (kataegis), exhibiting the C>T and C>G signature at TpC dinucleotides associated with APOBEC-mediated mutagenesis (Nik-Zainal et al., 2012a; Roberts et al., 2012; Roberts et al., 2013; Chan et al., 2015).

The mechanism of chromosome fragmentation that gives rise to chromothripsis in cancer is not known and it is not clear when, where, and how the DNA fragments are rejoined. A proposed explanation of the localized nature of chromothripsis is the sequestration of a chromosome (fragment) in a micronucleus where it is shattered while the rest of the genome remains intact (Zhang et al., 2015). Micronuclei in cancer cell lines show abnormalities in DNA replication, transcription, and nuclear envelope (NE) structure, and display DNA damage (reviewed in Hatch and Hetzer, 2015). Importantly, micronuclei show frequent nuclear envelope collapse, which could cause the aforementioned abnormalities (Hatch et al., 2013). Chromothripsis was recently shown to arise after rupture of micronuclei containing lagging chromosomes (Zhang et al., 2015). Therefore, a plausible scenario for the origin of chromothripsis involves a lagging chromosome (fragment), formation of a micronucleus that undergoes nuclear envelope collapse, DNA fragmentation due to impaired DNA replication, and random joining of the DNA fragments

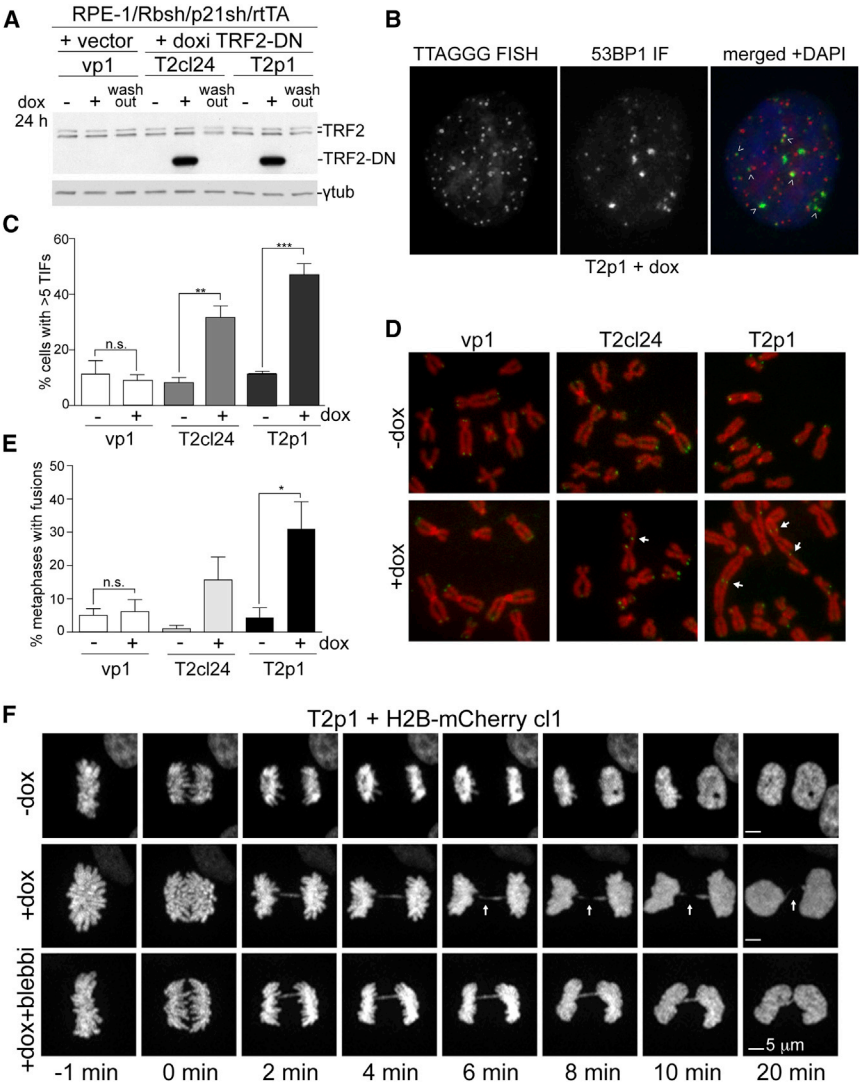

Figure 1. Dicentric Chromosomes Persist through Anaphase

(A) Immunoblotting for TRF2 and TRF2-DN 48 hr after dox in the indicated RPE-1 cell lines. Washout: 48 hr after removal of dox.

(B) Example of 53BP1 TIFs (arrows) in T2p1 48 hr after dox. Red: telomeric FISH; green: IF for 53BP1; blue: DAPI DNA stain.

(C) Quantification of TIFs as shown in (B). Bar graphs present mean values from three independent experiments (> 49 cells each) and SDs. **$p \leq 0.01$, ***; $p \leq 0.001$ (Student's t test).

(D) Metaphases with telomere fusions (arrows) in the indicated cells 48 hr after dox. Red: DAPI DNA stain; green: telomeric FISH.

(E) Quantification of telomere fusions as determined in (D). Data are means and SDs from three independent experiments (> 5600 telomeres per cell line per experiment). n.s., not significant; *$p \leq 0.05$ (Student's t test).

(F) Images of H2B-mCherry marked chromatin at the indicated time points from T2p1 with and without induction (+ and -dox) of telomere fusions with and without blebbistatin. Arrows (+dox images) highlight positions with absent H2B signals. See also related Figure S1 and Movie S1.

upon their incorporation into the primary nucleus (Zhang et al., 2015; Hatch and Hetzer, 2015).

Here, we present data suggesting a telomere-based mechanism for chromothripsis in cancer. Using inducible telomere crisis in vitro, we document chromothripsis and kataegis in half of the descendant clones sequenced. Dicentric chromosomes formed through telomere fusion persisted through mitosis and cytokinesis to form long chromatin bridges between the daughter cells. The DNA in the chromatin bridges became partially single-stranded due to attack by the major cytoplasmic 3′ nuclease, TREX1 (DNaseIII) (reviewed in Rice et al., 2015). TREX1 appeared to gain access to the bridge DNA during transient nuclear envelope rupture during interphase (NERDI), and its nucleolytic activity was required for the timely resolution of the chromatin bridges. After bridge resolution, the partially ssDNA generated by TREX1 rejoined the primary nuclei. We infer from sequence analysis of clones emerging from telomere crisis that the ssDNA is processed by APOBEC3A/B-mediated cytosine deamination (reviewed in Roberts and Gordenin, 2014), leading to kataegis, and that the DNA fragments are joined randomly to generate the hallmarks of chromothripsis.

RESULTS

An In Vitro Model for Telomere Crisis

To approximate telomere crisis in vitro, we generated a derivative of the hTERT expressing RPE-1 retinal pigment epithelial cell line in which the Rb and p53 pathways were disabled with shRNAs to Rb and p21 (see Table S1). To induce the telomere fusions typical of telomere crisis, we used a dox-inducible dominant negative allele of TRF2 (TRF2-DN), which deprotects telomeres and induces telomere fusions (van Steensel et al., 1998). As expected, doxycycline induced the 53BP1-containing telomere dysfunction-induced foci (TIFs; Takai et al., 2003), which are indicative of TRF2-DN-induced ATM kinase signaling (Karlseder et al., 1999); impaired proliferation; and generated metaphases with telomere fusions (Figures 1A–1E, S1A, and S1B). Whereas the dox-inducible clone T2cl24 showed infrequent fusions, a pool of TRF2-DN expressing cells (T2p1) showed telomere fusions in a large fraction of the metaphases, allowing cell biological experiments (Figures 1A–1E, S1B). Despite the frequent telomere fusions, the induced T2p1 cells formed micronuclei infrequently (Figure S1C).

Dicentric Chromosomes Persist through Mitosis and Cytokinesis

The behavior of dicentric chromosomes in mitosis was examined using spinning-disk confocal imaging of H2B-mCherry-marked

chromatin in induced T2p1 cells, which developed anaphase bridges in the majority of mitosis (Figure 2B) as expected since ~1% of the 92 telomeres in these cells undergo fusion (Figure S1B). The images obtained with these cells were similar to those described by McClintock (McClintock, 1938), showing apparent cleavage of the chromatin bridges immediately before or during cytokinesis (Figure 1F, S1D and S1E, Movie S1, panel 1). Imaging with myrPALM-mTurquoise2 to mark the plasma membrane (Zacharias et al., 2002) showed that the H2B signal was diminished only at the site of ingression (Figure S1D and S1E, Movie S1, panel 2), indicating that the disappearance of the H2B signal was likely due to the cleavage furrow pinching the chromatin. Indeed, when ingression was blocked with the actomyosin inhibitor blebbistatin (Straight et al., 2003), the dicentric chromosomes clearly remained intact (0/24 resolution events) (Figure 1F, Movie S1, panel 1). Thus, as is the case in budding yeast (Haber et al., 1984; Lopez et al., 2015; Hill and Bloom, 1989), mammalian dicentric chromosomes can withstand the forces of the mitotic spindle and do not break before cytokinesis. This result is not unexpected given that the spindle force (0.5–1.5 nN) is insufficient to break a mitotic chromosome, which can withstand at least 100 nN (Houchmandzadeh et al., 1997). Cells with dicentrics did not show a delay in their progression through mitosis (Figure S1F) although tubulin remained associated with the midbody slightly longer (Figures S1G and S1H, Movie S1, panel 3).

Dicentric Chromosomes Develop into Long Chromatin Bridges

To monitor the fate of the dicentric chromosomes after cytokinesis, we captured 108 adjacent fields by spinning-disk confocal imaging at 10 min intervals for 24–48 hr (Figures S2A and S2B). Computational joining of the fields (Preibisch et al., 2009) allowed ~1,000 cells to be followed for 2 days (Movie S2). This "stitching" microscopy of H2B-mCherry labeled cells showed that daughter cells migrated away from each other despite their connecting chromatin bridge (Figures 2A–2D, Movie S3). The chromatin bridges, which were detectable with YOYO-1 in fixed samples (Figure 2C), developed with high frequency and measured 50–200 μm before breaking (Figures 2B and 2D). The H2B-mCherry intensity on the bridges appeared diminished and the IF signals for histones H2A, H2B, and H4 were low (Figure S2C), suggesting the loss of nucleosomes, perhaps due to the stretching of the chromatin bridge (Bennink et al., 2001).

The chromatin bridges remained intact for 3–20 hr with a median persistence time of ~9.3 hr (Figure 2E). Bridge resolution was apparent from a sudden change in morphology, the rapid movement of bridge remnants toward the primary nuclei, and the rapid movement of the daughter cells away from each other (Movie S3). The primary nuclei were often heart-shaped with invaginations opposite from the chromatin bridge, suggesting that the fused chromosome(s) were pulling at the nuclear envelope (Figures 2A and 2C; S2D, Movie S3). After bridge resolution, a small tail of chromatin was observed that shortened and eventually disappeared, most likely because the nuclear envelope regained its rounded state (Figure S2E). In some cases the bridge remnant persisted until the next mitosis (see below). The chromatin bridges did not appear to give rise to micronuclei (0 out of >100 events scored).

To determine the timing of bridge resolution relative to the cell cycle stage of the connected cells, we examined mTurquoise2-RPA70 patterns in the primary nuclei. At the time of bridge rupture, most primary nuclei had diffusely distributed RPA, indicating that they were not yet in S phase. When >90% of the bridges were resolved at 20 hr, fewer than 20% of the primary nuclei showed the punctate RPA pattern indicative of S phase (Figure 2E and S3A–S3C). Therefore, most chromatin bridges were resolved before DNA replication in the primary nuclei. EdU labeling showed no signal on the bridge DNA, suggesting that the chromatin bridges did not undergo aberrant premature DNA replication (Figure 2F).

Chromatin Bridges Accumulate RPA-Coated ssDNA

Although the chromatin bridges resolved before the primary nuclei entered S phase, ~80% of the bridges contained RPA before and/or at the time of their resolution (Figures 2G, 2H, and S3A–S3F). IF for endogenous RPA32 and imaging of mTurquoise2-RPA70 showed a punctate pattern on the bridges that developed into bright domains just before resolution (Figures 2G, 2H, S3A, and S3B, Movie S3, panel 2).

After bridge resolution, the RPA-coated domains became embedded in the primary nucleus or persisted as short connected tails before joining a daughter nucleus after the next mitosis (Figures S3C–S3F). Once resolved, the bridge remnants showed the presence of γH2AX, 53BP1, and Mre11 (Figures S3G–S3I), indicating chromatinization of the DNA and activation of the DNA damage response.

RPA-coated chromatin bridges were also observed after deletion of the shelterin protein TIN2 from mouse cells (Takai et al., 2011). Furthermore, RPA accumulated on chromatin bridges induced by TRF2-DN in the HTC75-T4 cell line, which is derived from the human HT1080 fibrosarcoma cell line (Figures S4A–S4C) (van Steensel et al., 1998). Finally, RPA was present on chromatin bridges resulting from lagging chromosomes induced by either inhibition of the Mps1 kinase (Santaguida et al., 2010) or treatment with nocodazole (Figures S4D–S4G), suggesting that the formation of ssDNA is not a peculiarity of chromatin bridges formed by dicentrics resulting from telomere fusions.

Chromatin Bridges Have an Altered Nuclear Envelope

IF for the transmembrane nuclear envelope protein LAP2 showed that the chromatin bridges were surrounded by NE (Figures 3A and B). Similarly, BAF1, which binds chromatin and helps assemble the nuclear lamina, was detectable on the chromatin bridges (Figure S4F). In contrast, IF for Lamins A/C and B1; nuclear pore complexes (NPCs) (detected by mAb414 and α-TPR); and the NE proteins SUN1, SUN2, and MAD1 suggested that while the chromatin bridges contained an NE, its composition was altered (Figures 3C–3F and S4F). Specifically, the intensity of Lamin A/C and Lamin B1 staining gradually diminished as the bridges extended and several NE components (e.g., NPCs, SUN1/2, and MAD1) were not detectable (Figures 3C–3F and S4F). Interestingly, Lamin B1 was also depleted from the NE of the primary nuclei (Figure 3E).

Cells with Chromatin Bridges Undergo NERDI

Some of the cells with chromatin bridges appeared to transiently lose RPA from one of the primary nuclei with a concomitant

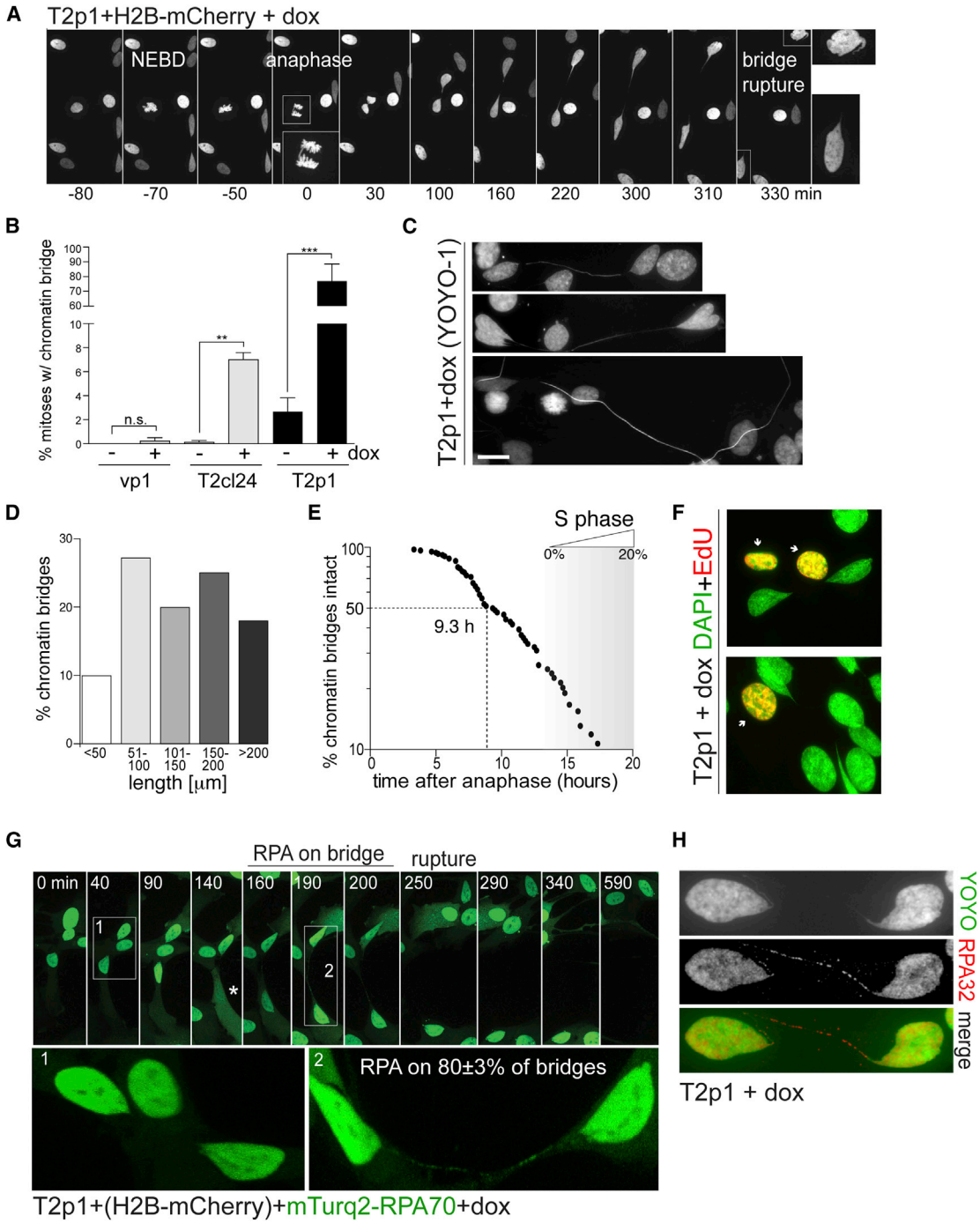

Figure 2. Dicentric Chromosomes form RPA-Containing Chromatin Bridges

(A) Images of chromatin from live-cell imaging of T2p1+H2B-mCherry treated with dox. Time points as indicated. NEBD: Nuclear envelope breakdown. Anaphase is shown in enlarged inset. The bridge resolves ~5.5 hr after anaphase. The images of the two daughter nuclei are enlarged on the right.

(B) Quantification of chromatin bridge induction derived from movies as in (A). Bar graphs represent the means and SDs of three independent experiments (> 50 cell divisions per experiment). n.s., not significant; **p ≤ 0.01 (Student's t test).

(C) Chromatin bridges with YOYO-1 DNA stain. Scale bar, 10 μm.

(D) Quantification of chromatin bridge length at resolution. Data derived from movies as in (A).

(E) Measurements of the timing of chromatin bridge resolution in h after anaphase. Data obtained from movies as in (A) (n = 84 from three independent experiments). Entry into S phase was based on RPA patterns. At 20 hr, ~20% of the cells are in S phase.

(F) Two examples of EdU staining (30 min pulse; red) and DAPI stain (green). Note the lack of EdU signal on the chromatin bridges and connected nuclei.

(legend continued on next page)

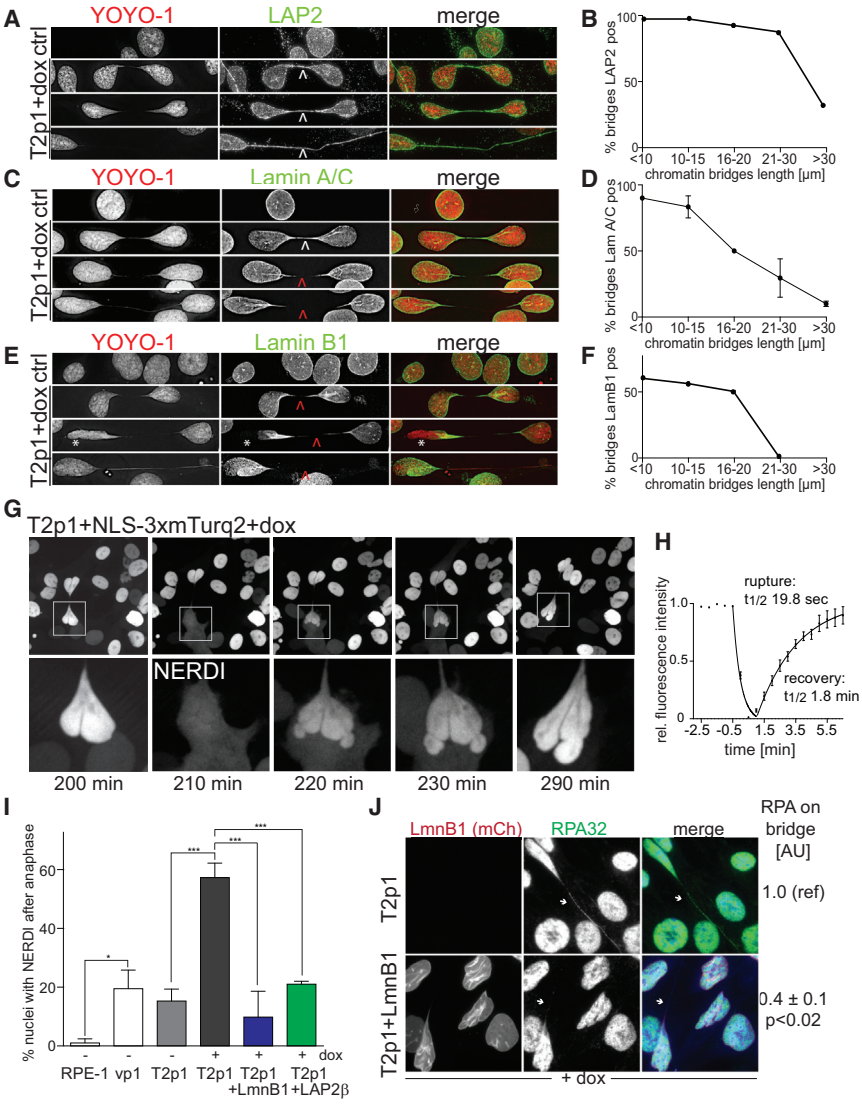

Figure 3. Transient NERDI Is Frequently Associated with Chromatin Bridges

(A, C, and E) IF for LAP2, Lamin A/C, or Lamin B1 IF (green) in T2p1 before and 48 hr after induction with dox. DNA stained with YOYO-1 (red). Arrows: white, signals present; red, signals undetectable. Asterisk: loss of Lamin B1 from NE of primary nucleus.

(B, D, and F) Quantification of LAP2, Lamin A/C, and Lamin B1 signals on chromatin bridges of the indicated length classes. Chromatin bridges were classified as positive if the IF signal was contiguous across the entire length of the bridge. Data from > 100 chromatin bridges in two independent experiments. Error bars: SEMs.

(G) Example of transient NERDI in cells with a chromatin bridge. NLS-3xmTurq2 images at the indicated time points from Movie S4. Bottom: enlargements of the transient NERDI.

(H) Duration of NERDI. Data obtained from movies generated with 30 s interval imaging on 10 cells as in (G). Error bars, SEMs.

(I) Quantification of the frequency of NERDI events occurring in at least one of the two daughter cells within 6 hr of anaphase before and after induction with dox. NERDI was assessed as in (G) but at 5 min intervals over 8 hr after anaphase. For the +dox samples, only cells with chromatin bridges were scored. Data from at least two experiments with > 40 anaphases each. *$p \leq 0.05$; ***$p \leq 0.001$ (one-way ANOVA with Tukey's correction for multiple comparisons). Error bars, SEMs.

(J) IF of RPA32 (green) with mCherry-Lamin B1 (red) and YOYO-1 stained DNA (blue) in cells with and without Lamin B1 overexpression. Arrows mark chromatin bridges. Note absence of RPA32 on the chromatin bridge in mCherry-Lamin B1 expressing cells. Numbers to the right show quantification (means ± SEMs) from > 40 chromatin bridges from two independent experiments. p value from Student's t test.

See also Figure S4 and Movie S4.

increase of the RPA signal in the cytoplasm (Figure 2G, asterisk). This mis-localization of RPA70 could be explained if the cells experienced NERDI. In micronuclei, NE collapse drives an irreversible loss of compartmentalization (Hatch et al., 2013), whereas in several cancer cell lines, NERDI of the main nucleus is transient (Vargas et al., 2012). Relevant to the anomalous Lamin B1 staining observed in nuclei connected by chromatin bridges (Figure 3E), Lamin B1 depletion exacerbates NERDI (Vargas et al., 2012).

To assay for NERDI, we used a fusion of three tandem copies of mTurquoise2 and the nuclear localization signal (NLS) of SV40 large T, which is confined to the nucleus when the NE is intact. Time-lapse imaging showed that cells with chromatin bridges had frequent and short-lived (~5 min) NERDI as evidenced by the appearance of cytoplasmic NLS-3xmTurq2 and its diminished intensity in the nucleus (Figures 3G and 3H; Movie S4). After NERDI, the nuclear envelope regained its integrity and retained the NLS-3xmTurq2 marker. Cells that did not contain TRF2-DN (vp1; Table S1) and non-induced T2p1 cells exhibited at least one NERDI event in 20% of daughter cell pairs within 6 hr of anaphase (Figure 3I). This high baseline rate of NERDI is likely due to p21 and/or Rb inactivation since NERDI was infrequent

(G) Accumulation of RPA on chromatin bridges before their resolution. T2p1+H2B-mCherry+mTurquoise2-RPA70 cells were examined by live-cell imaging. Stills showing the mTurquoise-RPA70 signal on one chromatin bridge are shown. Enlargements: bridge without and later with RPA70. 80% ± 3% of bridges (mean ± SD; 102 bridges from 3 independent experiments) contained RPA. Asterisk: apparent NERDI.

(H) IF for RPA32 (red) on fixed cells with a chromatin bridge. DNA stained with YOYO-1 (green).

See also Figure S2, S3, and S4, and Movies S2 and S3.

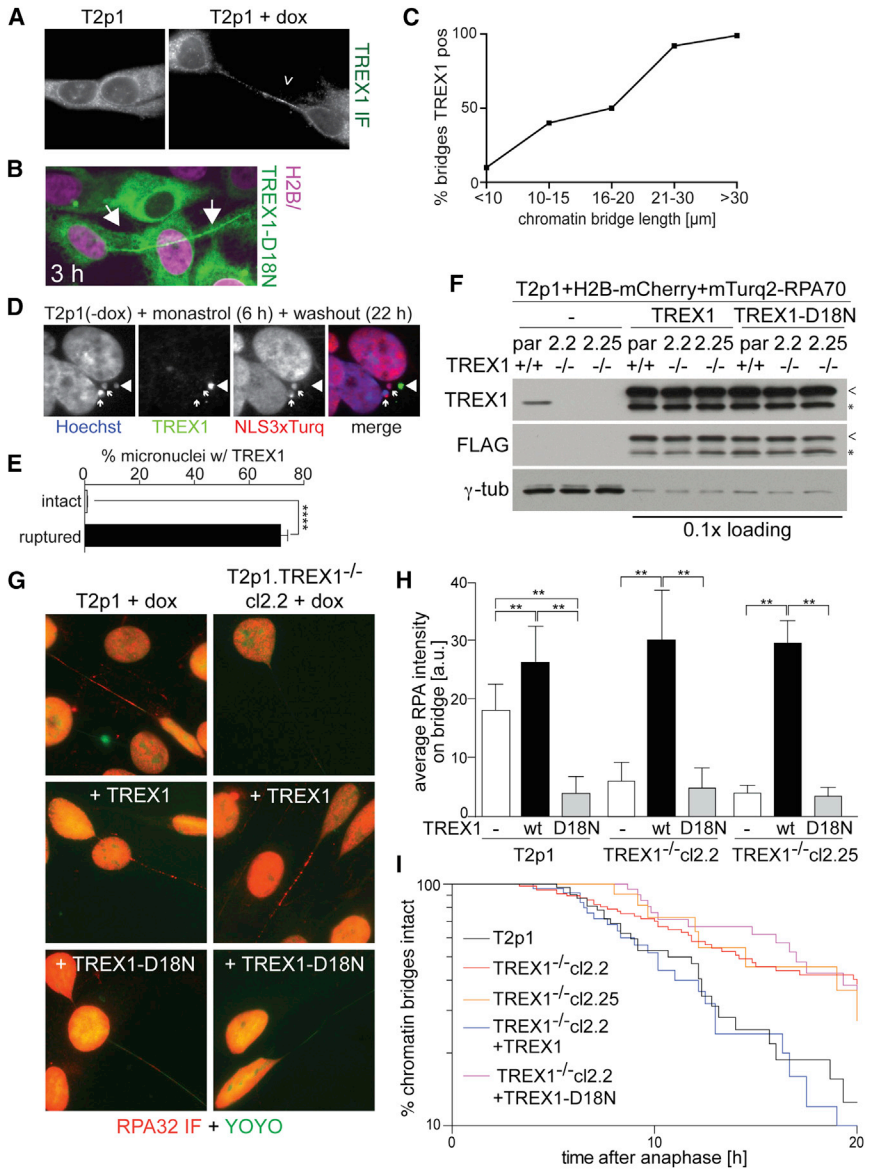

Figure 4. TREX1 Generates ssDNA in Chromatin Bridges and Promotes Resolution

(A) IF for TREX1 (white) on Tp21 cells with and without dox.

(B) Images from live-cell imaging of mTurq2-TREX1-D18N on a chromatin bridge (Movie S5).

(C) Quantification of TREX1 positive chromatin bridges of the indicated length classes. Positively scored chromatin bridges had at least five TREX1 foci. Data from three independent experiments with 100 chromatin bridges each.

(D) IF for TREX1 (green) in T2p1 cells with intact (NLS-3xTurq+; arrows) and disrupted (NLS-3xTurq-; arrowhead) micronuclei induced with monastrol.

(E) Quantification of TREX1 positive micronuclei as in (D). Over 300 micronuclei were analyzed from three independent experiments. ****$p \leq 0.0001$ (Student's t test). Error bars, SEMs.

(F) Immunoblotting for endogenous TREX1 and exogenous wild-type and mutant TREX1 (FLAG) in the indicated cell lines. Par: parental T2p1+ H2B-mCherry+mTurq2-RPA70 cells. Cl.2.2 and cl.2.25: TREX1 CRISPR KO clones. Arrowheads: full-length FLAG-TREX1. Asterisks: degradation products.

(G) Examples of the RPA32 IF in cells as in (F).

(H) Quantification of the RPA32 IF intensity on chromatin bridges in cells as in (F). Data were obtained from 55 chromatin bridges from three independent experiments. Bars indicate SDs. **$p \leq 0.01$ (Student's t test).

(I) Timing of chromatin bridge resolution after anaphase in the indicated cell lines. See legend to Figure 2E.

See also related Figure S4 and S5 and Movie S5.

in the parental RPE1-hTERT cells (Figure 3I). Importantly, NERDI frequency increased to nearly 60% in dox-induced T2p1 daughter cells with chromatin bridges (Figure 3I). NERDI usually occurred in one of the two connected nuclei. Because NERDI can be induced by Lamin B1 depletion (Vargas et al., 2012), we tested whether Lamin B1 or LAP2β overexpression could repress the nuclear envelope rupture in induced Tp21 cells (Figure 3I). Overexpression of both proteins diminished the frequency of NERDI (Figure 3I). Lamin B1 overexpression strongly diminished RPA accumulation on chromatin bridges suggesting that the formation of ssDNA on chromatin bridges depended on NERDI (Figure 3J). We conclude that telomere dysfunction in this cell system induces a significant increase in NERDI. As a result, at least one of the two cells connected by a chromatin bridge is likely to experience a NERDI event within the time period preceding bridge resolution.

Chromatin Bridge DNA Is Processed by the Cytoplasmic 3′ Exonuclease TREX1

Although we initially queried nuclear nucleases, the frequent NERDI suggested that a cytoplasmic nuclease might attack the chromatin bridges to generate ssDNA. IF showed that the major cytoplasmic 3′ exonuclease TREX1 was present on the chromatin bridges in cells undergoing telomere crisis, whereas TREX1 was only observed in the cytoplasm of control cells (Figure 4A). TREX1 also localized to chromatin bridges induced by telomere dysfunction in the HTC75-T4 cell line and to chromatin bridges formed by lagging chromosomes induced by nocodazole (Figures S4A and S4G). IF analysis and imaging of the inactive mTurq2-tagged TREX1-D18N (Lehtinen et al., 2008) indicated that this nuclease often appears on the chromatin bridges before their rupture (Figures 4B and 4C, Movie S5). IF for TREX1 in micronuclei induced by monastrol also showed TREX1 accumulation specifically in micronuclei that had undergone NE rupture (Figures 4D and 4E).

To test the role of TREX1 in the generation of ssDNA, we used CRISPR/Cas9 to derive TREX1 KO subclones from the T2p1 telomere crisis cell line (Figures S5A and S5B). Loss of TREX1

was demonstrated by immunoblotting and IF (Figure 4F, S5C, and S5D), and sequence analysis revealed bi-allelic CRISPR gene editing (Figure S5E). The TREX1 KO cell lines showed normal proliferation and, after induction of TRF2-DN, displayed the expected reduced proliferation and chromatin bridges (Figures S5F and S5G). Importantly, IF showed a nearly complete abrogation of the accumulation of RPA on the chromatin bridges in the TREX1 KO cells (Figures 4G and 4H). This absence of RPA accumulation could be reversed by reintroduction of wild-type TREX1, whereas the inactive TREX1-D18N did not have this effect (Figures 4F–4H). Consistent with a previous report (Lehtinen et al., 2008), TREX1-D18N had a dominant-negative effect in the TREX1-proficient parental cell line, significantly reducing the appearance of RPA on the chromatin bridges (Figures 4F–4H). In contrast, overexpression of the wild-type allele in the parental Tp21 cell line slightly increased the accumulation of RPA on the chromatin bridges. As a control, we confirmed that TREX1 deficiency did not diminish RPA foci formed during replication stress (Figures S5H and S5I).

TREX1 deletion from the HTC75-T4 cell line also strongly diminished RPA accumulation on chromatin bridges (Figures S4B and S4C). Furthermore, chromatin bridges resulting from lagging chromosomes induced by Mps1 kinase inhibition failed to accumulate RPA when TREX1 was absent (Figures S4D–S4F). Thus, TREX1 deficiency generally affects the formation of RPA-containing ssDNA in chromatin bridges.

Cells lacking TREX1 showed a significant delay in the resolution of chromatin bridges (Figure 4I). At 20 hr post-anaphase, only 15% of the chromatin bridges in the TREX1-proficient cells remained, whereas more than 40% of the bridges of the TREX1 KO cell line were still intact. The timing of bridge resolution was restored by wild-type TREX1, but not by TREX1-D18N. TREX1-independent mechanisms also contribute to the resolution of the chromatin bridges, since resolution was not abrogated by TREX1 deficiency.

Frequent Chromothripsis in Post-crisis Clones

To determine the genetic alterations induced by telomere crisis, we isolated post-crisis subclones of T2p1 and T2cl24. Clones were karyotyped to exclude those that had escaped the telomere dysfunction (Figure S6 and Table S2). Clones with aneuploidy and/or marker chromosomes were analyzed by telomere fusion PCR to confirm the presence of telomere fusion (Figure S6C). Ten such post-crisis clones were selected for sequence analysis, as were the parental T2p1, one post-crisis subclone with the parental karyotype (24.2), and seven control subclones derived from uninduced T2p1 cells. We performed whole-genome sequencing on all 19 lines, comparing post-crisis whole-genome sequencing data with that from the parental lines, in order to identify mutations acquired during telomere crisis. None of the subclones derived from the uninduced T2p1 cells showed genomic alterations.

Strikingly, five of ten post-telomere crisis lines showed clusters of genomic rearrangements affecting one or more chromosomes (Figures 5 and S7A). These rearrangements exhibited the hallmarks of chromothripsis, including spatial clustering, randomness of fragment orientation and oscillating copy-number states (Figures 5A, 5B, and S7A) (Korbel and Campbell, 2013). In several examples, the rearrangements were near telomeres and associated with terminal deletions of the chromosome, consistent with products of telomere fusion. Chromothripsis events that are more internal in the chromosomes can also result from telomere fusions since the genomic region in the bridge could be far from the telomere depending on the structure of the dicentric. Sometimes the clustered rearrangements affected one chromosome, sometimes two or three, as has been observed in cancers (Stephens et al., 2011). Importantly, chromothripsis never involved whole chromosomes but rather was localized to specific regions that presumably resided in the chromatin bridge. Consistent with these results, chromothripsis was recently reported in cells that were subjected to TRF2 inhibition and an Mps1 kinase inhibitor (Mardin et al., 2015).

The oscillations of copy number in regions of apparent chromothripsis often sampled three copy-number states. Such a scenario can arise either from a chromothripsis event simultaneously affecting two copies of the same genomic region or from a subsequent duplication of part of a chromothripsis chromosome. These two possibilities can be distinguished by the patterns of copy-number changes across breakpoints in the region (Li et al., 2014). In all examples observed here, the patterns of copy number and rearrangements implied that two copies of the affected genomic regions were simultaneously subjected to the catastrophic shattering and repair of chromothripsis (Figures 5 and S7). Two copies could derive from the end-to-end fusion of sister chromatids that form the chromatin bridge.

Kataegis Accompanies Chromothripsis

The recruitment of RPA suggested that chromatin bridges contain extensive ssDNA. As ssDNA represents one of the target substrates for APOBEC enzymes, we hypothesized that the regions caught up in the chromatin bridge would show clusters of point mutations, known as kataegis, analogous to those seen in cancers (Nik-Zainal et al., 2012a; Nik-Zainal et al., 2012b; Roberts et al., 2012).

We observed 29 clusters of point mutations from seven of the ten post-crisis samples sequenced here that were absent from the parental cell lines. These clusters exhibited the cardinal features of kataegis observed in human cancers. First, clusters were often found within a kilobase or two of genomic breakpoints (Figures 6A–6D). These were predominantly in association with chromothripsis rearrangements, although occasional clusters were also found near simpler structural variants (Figure 6C). Second, the clusters exhibited a pronounced preference for C>T and C>G mutations occurring in a TpC context (Figures 6E and 6F), the classic signature of APOBEC3A/B activity (Roberts et al., 2013; Burns et al., 2013a; Burns et al., 2013b; reviewed in Roberts and Gordenin, 2014). Third, the mutation clusters were processive, indicative of the damage occurring on a single strand of DNA (Figures 6A and 6B).

DISCUSSION

The findings reported here suggest that chromothripsis and kataegis can arise as a consequence of telomere crisis in the early stages of human tumorigenesis (Figure 7). The dicentric

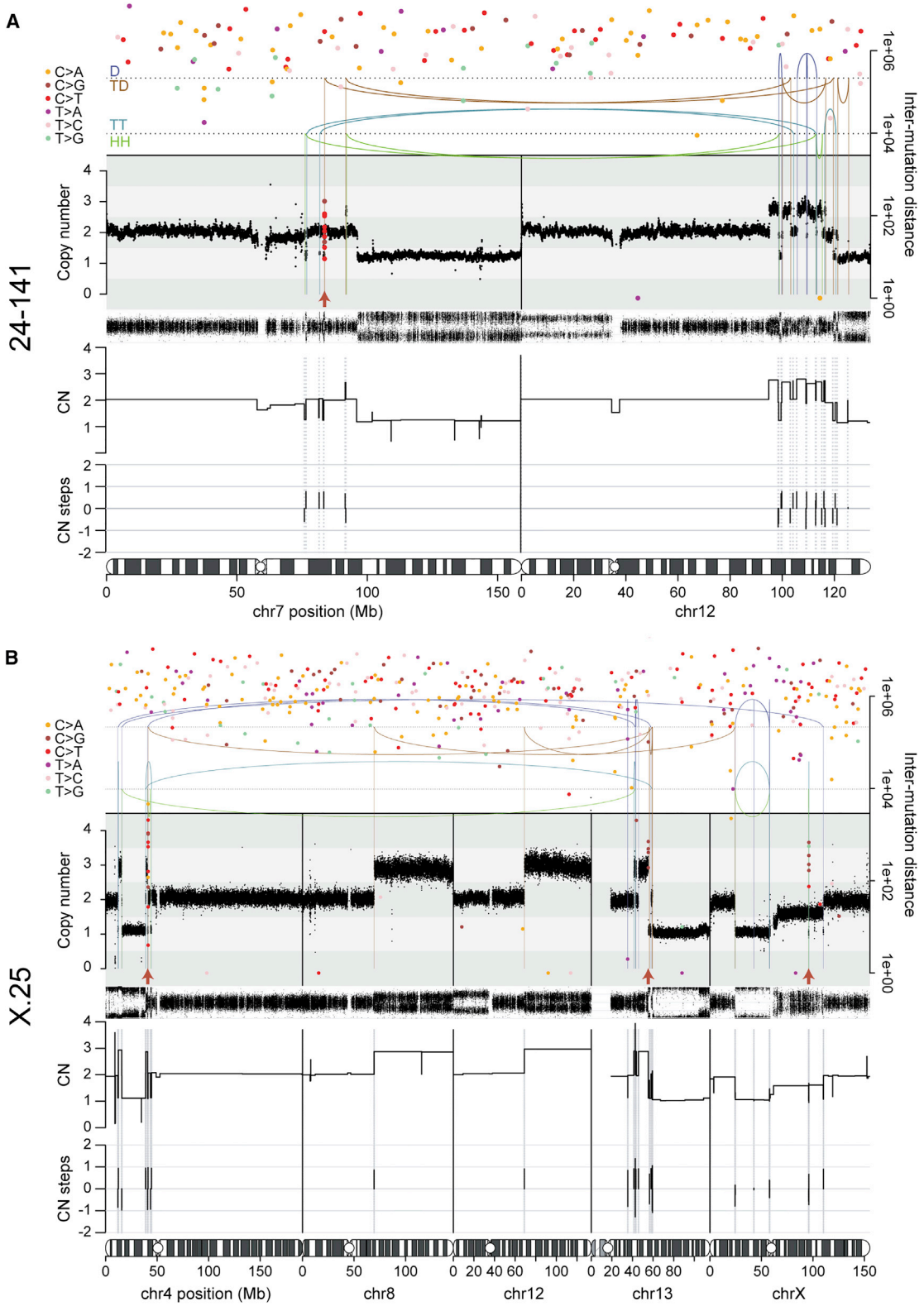

(legend on next page)

chromosomes formed in telomere crisis developed into long chromatin bridges that connect the two primary nuclei until the bridge breaks. Three important events in cells with chromatin bridges can explain the observed chromothripsis and kataegis. First, one of the connected primary nuclei undergoes NERDI that allows entry of the cytoplasmic 3′ exonuclease TREX1. Second, TREX1 generates extensive ssDNA in the chromatin bridges. Third, TREX1-mediated processing contributes to the resolution of the bridge, leaving two bridge DNA remnants that each join their primary nucleus. Subsequent repair of the bridge remnant DNA results in random joining of DNA segments typical of chromothripsis. In addition, APOBEC-derived hypermutation is prominent at the boundaries of the rearranged sequences. Since APOBEC enzymes act on ssDNA, the observed kataegis is consistent with the extensive single-stranded nature of the bridge remnants.

Complex clusters of structural variants have been observed in many cancer genomes. Chromothripsis is an extreme example of such clusters, with tens to hundreds of genomic rearrangements affecting one or a few chromosomes or chromosome regions. Especially high rates have been observed in sarcomas, esophageal cancers, and neuroblastomas (Nones et al., 2014; Stephens et al., 2011; Garsed et al., 2014; Mehine et al., 2013), and there appears to be an association with telomere crisis, especially BFB cycles (Li et al., 2014). Our study strengthens this association, suggesting that one of the routes to the chromosome damage that precipitates chromothripsis could be chromatin bridges formed by dicentric chromosomes.

While this study suggests that telomere crisis can precipitate chromothripsis events in cancer, many mechanistic questions remain. These issues are briefly discussed below.

Formation of Extended Chromatin Bridges

Chromatin bridges have been documented and observed numerous times upon induction of telomere fusions in a wide variety of cell lines, but their significance, duration, and eventual fate had not been determined. In all cases, the chromatin bridges were observed in adherent tissue culture cells. We do not know whether chromatin bridges also develop if cells are grown in soft agar or indeed if such bridges would occur when incipient cancer cells undergo telomere crisis in vivo. Presumably, cell migration is not limited to tissue culture settings and takes place in the mass of cells that eventually gives rise to overt cancer. Cell motility is well documented in wound healing and is promoted by the epithelial-mesenchymal transition (EMT) in cancers of epithelial origin (Scheel and Weinberg, 2012). Furthermore, modeling suggests that cell migration is an important contributor to cancer development (Waclaw et al., 2015).

NERDI in Cells with Chromatin Bridges

In cells with chromatin bridges, NERDI is more frequent and occurs sooner after anaphase. What is the mechanism by which chromatin bridges induce NERDI? One possibility is that the long bridges simply deplete critical NE components (e.g., Lamin B1, Lamin A/C) from the primary nuclei, thus inducing the transient failure in compartmentalization. A second possibility is that the stretching of the bridge exerts mechanical forces on the primary nuclei that overwhelm the resilience of the NE. Indeed, the shape of many of the primary nuclei suggests that considerable pulling forces are exerted by the chromosome(s) in the bridge, but further work is required to understand the exact mechanism by which NERDI occurs. The attachment of human chromosomes to the nuclear lamins (Guelen et al., 2008) could play a role in generating the observed distortions and contribute to NERDI induction.

Preferential TREX1 Action on Bridge DNA

Why does TREX1 accumulate on the bridge and attack the bridge DNA rather than affecting the chromatin of the primary nucleus undergoing NERDI? One explanation could be that the bridge DNA is in a non-canonical chromatin state. It is possible that the pulling force of the migrating daughter cells results in loss of nucleosomes from the chromatin in the bridge (reviewed in Chien and van Noort, 2009). This mechanical nucleosome removal is consistent with the diminished staining for histones on the chromatin bridges. If TREX1 preferentially binds naked dsDNA, it would be expected to accumulate more on the non-nucleosomal bridge DNA than on the chromatin in the primary nucleus. Indeed, TREX1 degrades naked DNA much faster than nucleosomal DNA (Chowdhury et al., 2006), but whether this effect is due a higher affinity for naked DNA is not known.

Since TREX1 is a 3′ exonuclease, it will require nicked DNA substrates for the generation of ssDNA. Indeed, TUNEL staining has previously shown free 3′ ends on a chromatin bridge (Gisselsson et al., 2001). The nicks in the bridge DNA could originate from RNaseH2-mediated removal of misincorporated ribonucleotides (Reijns et al., 2012). Another possibility is that the TREX1-associated endonuclease NM23-H1 generates the 3′ ends used by the exonuclease (Chowdhury et al., 2006). So far, we have failed to detect NM23-H1 on the chromatin bridges but its abundance there may simply be too low for detection.

Bridge Resolution

Bridge resolution is strongly correlated with a sudden increase in RPA staining, suggesting that the formation of ssDNA is a critical step. In the absence of TREX1, no or very low amounts of RPA

Figure 5. Chromothripsis and Kataegis in Post-Crisis Clones 24-141 and X-25

(A) Chromothripsis and rainfall plot of sample 24-141 involving chromosomes 7 and 12.

(B) Chromothripsis and rainfall plot of sample X-25 involving chromosomes 4, 13 and X. The unbalanced rearrangements involving chromosomes 8 and 12 may have taken place together with the chromothripsis event. In (A) and (B), top: the arcs represent the two ends of rearrangements. Arcs are grouped from top to bottom by the type of rearrangement orientation as follows: deletion (D; +-); tandem duplication (TD; -+); tail-tail (TT; ++); head-head (HH;–). Middle: estimated copy number over genomic windows. The variant allele frequency (VAF) track is shown below the copy-number track. Inferred copy-number segments are shown below the VAF track. Bottom: amount of copy-number change between copy-number segments. Chromothripsis after a duplication will yield three copy-number states with copy-number steps of +1 or –1. Duplication after chromothripsis will yield some copy-number steps of +2 or –2. Filled circles: positions of point mutations colored by mutation type. The y axis shows the distance of each mutation to the next on the same chromosome, with the respective axis on the right-hand side of the graph. Red arrows: kataegis clusters.

See also related Figure S6 and S7.

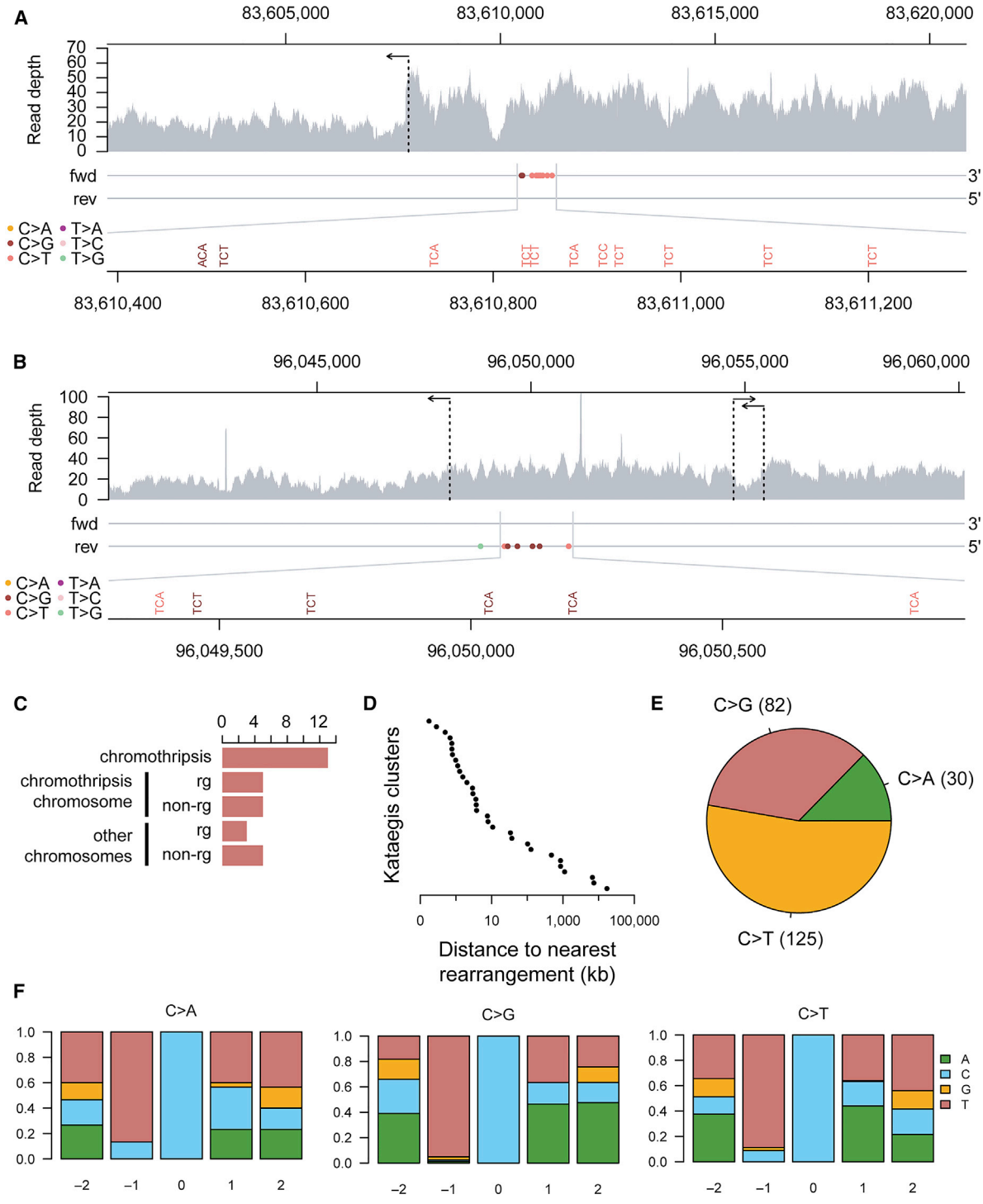

Figure 6. Mutational Patterns of Kataegis in Post-Crisis Clones

(A) A chromothripsis-associated kataegis in sample 24-141 on chromosome 7.

(B) A kataegis event in sample X-25 on chromosome X. This kataegis event took place on a chromosome with evidence for chromothripsis, but the rearrangements associated with the kataegis event do not appear to be part of the chromothripsis (Figure 5B). For both (A) and (B), the top panel shows raw read coverage of the region. The horizontal arrows indicate the positions of rearrangements. The two horizontal lines in the middle panel represent the forward and reverse strands. The pyrimidine strands of the mutations called are indicated by their placement on one of the two strands. Mutations are colored by mutation type. The bottom panel magnifies the mutation cluster regions and shows mutation contexts.

(C) The number of kataegis events grouped by their association with rearrangements as follows. From top to bottom: kataegis events within 10 kb of a chromothripsis rearrangement; kataegis events on a chromothripsis chromosome within 10 kb of a non-chromothripsis rearrangement; kataegis events on a

(legend continued on next page)

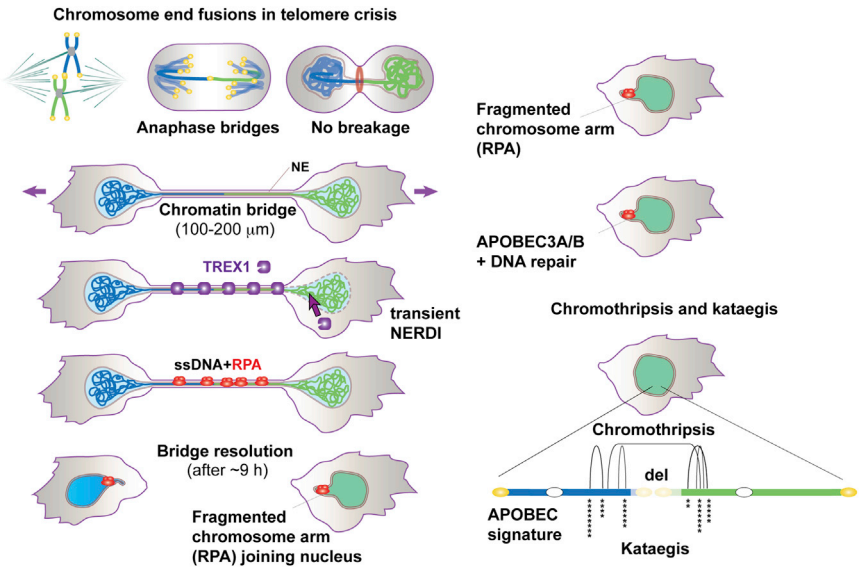

Figure 7. The Fate of Dicentric Chromosomes Formed in Telomere Crisis

Telomere fusions in telomere crisis give rise to anaphase bridges that persist and develop into chromatin bridges. Cells with chromatin bridges undergo frequent NERDI and TREX1 accumulates on the chromatin bridge. TREX1 generates RPA-marked ssDNA in the chromatin bridge before their resolution. The RPA marked bridge remnants eventually join the primary nucleus where DNA repair and APOBEC3A/B editing are inferred to take place. Clonal descendants derived from telomere crisis cells show chromothripsis and kataegis.

are detected on the chromatin bridges. The residual RPA staining could be due to another nuclease or could be due to the over-stretching of the DNA, which can lead to RPA-coated denatured DNA in vitro (van Mameren et al., 2009). Although TREX1 is not solely responsible for bridge resolution, it significantly enhances the resolution of the bridges. We imagine that resolution occurs when two TREX1 3′ exonucleases acting on the Watson and Crick strands meet.

CONCLUSIONS

Telomere crisis has previously been shown to give rise to aneuploidy, non-reciprocal translocations, and whole-genome reduplication (Artandi et al., 2000; Davoli and de Lange, 2012; Davoli et al., 2010). The data presented here suggest that chromothripsis and kataegis can be added to the list of cancer-relevant genome alterations that could be the consequence of telomere crisis. It will therefore be of interest to develop better tools to detect telomere crisis in the early stages of cancer. Methods to detect telomere crisis in pre-cancerous lesions may have predictive power with regard to disease progression and outcome.

EXPERIMENTAL PROCEDURES

Additional experimental procedures are available in Supplemental Information.

Cell Culture Procedures and Plasmids

RPE1-hTERT and Phoenix cells from the American Type Culture Collection (ATCC) were cultured as described by the ATCC. Drug treatments, retroviral transduction, and cell cloning were performed using standard conditions (see Supplemental Experimental Procedures). CRISPR/Cas9 knockouts were generated with sgTREX1-2, 5′-GAGC CCCCCCACCTCTC-(PAM)-3′ using the gRNA cloning vector (Addgene) and co-transfection with an hCas9 plasmid (Addgene) by nucleofection (Lonza apparatus). Clones were isolated by limiting dilution, screened for TREX1 deletion by immunoblotting, and sequenced.

Immunoblotting and Immunofluorescence

Immunoblotting and IF were performed using standard protocols. Cells were incubated with EdU for 30 min prior to PFA fixation and EdU detection with a Click-iT EdU Alexa Fluor 647 imaging kit (Life Technologies).

Live-Cell Imaging

Cells were plated onto 35 mm glass bottom dishes (MatTek) 48 hr before imaging. One hour before imaging, the media was replaced with phenol red-free DMEM/F12 medium. Live-cell imaging was performed at 37°C and 5% CO_2 using a CellVoyager CV1000 spinning-disk confocal system (Yokogawa, Olympus) equipped with 445, 488, and 561 nm lasers, a Hamamatsu 512 × 512 EMCCD camera, and pinhole size of 50 μm. Details of image acquisition, processing, and quantification are given in the Supplemental Information.

Telomere Fusion PCR and Karyotypic Analysis

PCR for telomeric fusions and metaphase telomere fusion assays were performed essentially as described (Letsolo et al., 2010; Capper et al., 2007). Karyotypes were determined using standard protocols.

X-ten Sequencing and Mapping

Genomic DNA sequencing libraries were synthesized on robots and cluster generation and sequencing were performed using the manufacturer pipelines. Average sequence coverage across the samples was 33.3x (range, 27.4–35.9x). Mapping to genome build hs37d5 was performed using the BWA algorithm (BWA mem 0.7.8 (Li and Durbin, 2010)).

Copy-Number Analysis

The reference genome divided into windows of equivalent read numbers (Campbell et al., 2008; Li et al., 2009) was used to extract reads with a mapping quality of at least 35 and the following flags: Properly paired; non-secondary;

chromothripsis chromosome with no rearrangements within 10 kb; kataegis events on a non-chromothripsis chromosome within 10 kb of a rearrangement; and kataegis events on non-chromothripsis chromosome with no rearrangements within 10 kb.
(D) The distance of each of the 31 detected kataegis events to their nearest respective rearrangement breakpoint.
(E) The frequency distribution of mutation types in the detected kataegis clusters.
(F) The nucleotide context around the mutated cytosine grouped by cytosine mutation type. The relative positions shown are on the pyrimidine (cytosine) strand. The Y-axes show the fraction of each nucleotide on the pyrimidine strand.
See also related Figure S7.

QC-pass; non-duplicate; non-supplementary. Reads overlapping with each window were counted using BEDTools (Quinlan, 2014) and copy numbers were inferred from read depth data (Li et al., 2014).

Rearrangement Calling and Chromothripsis

Clusters of abnormally paired read pairs were identified from the merged sequence data using an in-house algorithm "Brass." Raw rearrangement calls supported by clusters of abnormally mapped read pairs were called if the clusters were formed of at least four read pairs all from the same sample. For X-37, which yielded noisier data, at least six read pairs were required. The raw rearrangements were filtered as described previously (Li et al., 2014).

Mutation Calling and Kataegis

Point mutations were called using an in-house algorithm "Caveman" as before (Nik-Zainal et al., 2012a) with RPE-1/Rbsh/p21sh/rtTA (Table S1) as reference. Raw mutations filtering is described in the Supplemental Information. Kataegis mutation clusters were detected using visual inspection based on the criteria of short inter-mutation distance (generally <2 kb) between cytosine mutations that were processive and enriched with TpC context.

ACCESSION NUMBERS

The accession number for the genome sequence data reported in this paper is European Genome-Phenome Archive (http://www.ebi.ac.uk/ega/, hosted by the EBI): EGAD00001001629 (https://www.ebi.ac.uk/ega/datasets/EGAD00001001629).

SUPPLEMENTAL INFORMATION

Supplemental Information includes Supplemental Experimental Procedures, seven figures, two tables, and five movies and can be found with this article online at http://dx.doi.org/10.1016/j.cell.2015.11.054.

AUTHOR CONTRIBUTIONS

J.M. and T.d.L. designed the experiments. J.M. performed all the cell biological experiments with the help of N.B. Y.L. and P.J.C. performed the genomic analysis on clones derived by J.M. and N.B. T.d.L. and P.J.C. wrote the paper with the help of the other authors.

ACKNOWLEDGMENTS

We thank Prasad Jallepalli for reagents, Martin Hetzer for discussion, and Zhe Yang for performing PCR validation of chromothriptic breakpoints. We thank S. Yu and the de Lange lab for discussion and help with this manuscript. P. Ariel, T. Tong, and A. North of the RU Bio-imaging Core Facility provided expert assistance with microscopy. The MSKCC Cytogenetics Core acknowledges NIH Cancer Center grant P30 CA008748. J.M. is a Merck Fellow of The Jane Coffin Childs Memorial Fund for Medical Research. Work in P.J.C.'s lab was supported by the Wellcome Trust (077012/Z/05/Z), and P.J.C. holds a Wellcome Trust Senior Clinical Fellowship (WT088340MA). This work was supported by grants from the NCI (5R01CA181090) and the Breast Cancer Research Foundation to T.d.L. T.d.L. is an American Cancer Society Research Professor.

Received: August 18, 2015
Revised: November 3, 2015
Accepted: November 20, 2015
Published: December 17, 2015

REFERENCES

Artandi, S.E., and DePinho, R.A. (2010). Telomeres and telomerase in cancer. Carcinogenesis *31*, 9–18.

Artandi, S.E., Chang, S., Lee, S.L., Alson, S., Gottlieb, G.J., Chin, L., and DePinho, R.A. (2000). Telomere dysfunction promotes non-reciprocal translocations and epithelial cancers in mice. Nature *406*, 641–645.

Bennink, M.L., Leuba, S.H., Leno, G.H., Zlatanova, J., de Grooth, B.G., and Greve, J. (2001). Unfolding individual nucleosomes by stretching single chromatin fibers with optical tweezers. Nat. Struct. Biol. *8*, 606–610.

Bignell, G.R., Santarius, T., Pole, J.C., Butler, A.P., Perry, J., Pleasance, E., Greenman, C., Menzies, A., Taylor, S., Edkins, S., et al. (2007). Architectures of somatic genomic rearrangement in human cancer amplicons at sequence-level resolution. Genome Res. *17*, 1296–1303.

Burns, M.B., Lackey, L., Carpenter, M.A., Rathore, A., Land, A.M., Leonard, B., Refsland, E.W., Kotandeniya, D., Tretyakova, N., Nikas, J.B., et al. (2013a). APOBEC3B is an enzymatic source of mutation in breast cancer. Nature *494*, 366–370.

Burns, M.B., Temiz, N.A., and Harris, R.S. (2013b). Evidence for APOBEC3B mutagenesis in multiple human cancers. Nat. Genet. *45*, 977–983.

Campbell, P.J., Stephens, P.J., Pleasance, E.D., O'Meara, S., Li, H., Santarius, T., Stebbings, L.A., Leroy, C., Edkins, S., Hardy, C., et al. (2008). Identification of somatically acquired rearrangements in cancer using genome-wide massively parallel paired-end sequencing. Nat. Genet. *40*, 722–729.

Campbell, P.J., Yachida, S., Mudie, L.J., Stephens, P.J., Pleasance, E.D., Stebbings, L.A., Morsberger, L.A., Latimer, C., McLaren, S., Lin, M.L., et al. (2010). The patterns and dynamics of genomic instability in metastatic pancreatic cancer. Nature *467*, 1109–1113.

Capper, R., Britt-Compton, B., Tankimanova, M., Rowson, J., Letsolo, B., Man, S., Haughton, M., and Baird, D.M. (2007). The nature of telomere fusion and a definition of the critical telomere length in human cells. Genes Dev. *21*, 2495–2508.

Chan, K., Roberts, S.A., Klimczak, L.J., Sterling, J.F., Saini, N., Malc, E.P., Kim, J., Kwiatkowski, D.J., Fargo, D.C., Mieczkowski, P.A., et al. (2015). An APOBEC3A hypermutation signature is distinguishable from the signature of background mutagenesis by APOBEC3B in human cancers. Nat. Genet. *47*, 1067–1072.

Chien, F.T., and van Noort, J. (2009). 10 years of tension on chromatin: results from single molecule force spectroscopy. Curr. Pharm. Biotechnol. *10*, 474–485.

Chowdhury, D., Beresford, P.J., Zhu, P., Zhang, D., Sung, J.S., Demple, B., Perrino, F.W., and Lieberman, J. (2006). The exonuclease TREX1 is in the SET complex and acts in concert with NM23-H1 to degrade DNA during granzyme A-mediated cell death. Mol. Cell *23*, 133–142.

Davoli, T., and de Lange, T. (2012). Telomere-driven tetraploidization occurs in human cells undergoing crisis and promotes transformation of mouse cells. Cancer Cell *21*, 765–776.

Davoli, T., Denchi, E.L., and de Lange, T. (2010). Persistent telomere damage induces bypass of mitosis and tetraploidy. Cell *141*, 81–93.

Forment, J.V., Kaidi, A., and Jackson, S.P. (2012). Chromothripsis and cancer: causes and consequences of chromosome shattering. Nat. Rev. Cancer *12*, 663–670.

Garsed, D.W., Marshall, O.J., Corbin, V.D., Hsu, A., Di Stefano, L., Schröder, J., Li, J., Feng, Z.P., Kim, B.W., Kowarsky, M., et al. (2014). The architecture and evolution of cancer neochromosomes. Cancer Cell *26*, 653–667.

Gisselsson, D., Jonson, T., Petersén, A., Strömbeck, B., Dal Cin, P., Höglund, M., Mitelman, F., Mertens, F., and Mandahl, N. (2001). Telomere dysfunction triggers extensive DNA fragmentation and evolution of complex chromosome abnormalities in human malignant tumors. Proc. Natl. Acad. Sci. USA *98*, 12683–12688.

Guelen, L., Pagie, L., Brasset, E., Meuleman, W., Faza, M.B., Talhout, W., Eussen, B.H., de Klein, A., Wessels, L., de Laat, W., and van Steensel, B. (2008). Domain organization of human chromosomes revealed by mapping of nuclear lamina interactions. Nature *453*, 948–951.

Haber, J.E., Thorburn, P.C., and Rogers, D. (1984). Meiotic and mitotic behavior of dicentric chromosomes in Saccharomyces cerevisiae. Genetics *106*, 185–205.

Hatch, E.M., and Hetzer, M.W. (2015). Linking Micronuclei to Chromosome Fragmentation. Cell *161*, 1502–1504.

Hatch, E.M., Fischer, A.H., Deerinck, T.J., and Hetzer, M.W. (2013). Catastrophic nuclear envelope collapse in cancer cell micronuclei. Cell *154*, 47–60.

Hill, A., and Bloom, K. (1989). Acquisition and processing of a conditional dicentric chromosome in Saccharomyces cerevisiae. Mol. Cell. Biol. *9*, 1368–1370.

Houchmandzadeh, B., Marko, J.F., Chatenay, D., and Libchaber, A. (1997). Elasticity and structure of eukaryote chromosomes studied by micromanipulation and micropipette aspiration. J. Cell Biol. *139*, 1–12.

Karlseder, J., Broccoli, D., Dai, Y., Hardy, S., and de Lange, T. (1999). p53- and ATM-dependent apoptosis induced by telomeres lacking TRF2. Science *283*, 1321–1325.

Kloosterman, W.P., and Cuppen, E. (2013). Chromothripsis in congenital disorders and cancer: similarities and differences. Curr. Opin. Cell Biol. *25*, 341–348.

Korbel, J.O., and Campbell, P.J. (2013). Criteria for inference of chromothripsis in cancer genomes. Cell *152*, 1226–1236.

Lehtinen, D.A., Harvey, S., Mulcahy, M.J., Hollis, T., and Perrino, F.W. (2008). The TREX1 double-stranded DNA degradation activity is defective in dominant mutations associated with autoimmune disease. J. Biol. Chem. *283*, 31649–31656.

Letsolo, B.T., Rowson, J., and Baird, D.M. (2010). Fusion of short telomeres in human cells is characterized by extensive deletion and microhomology, and can result in complex rearrangements. Nucleic Acids Res. *38*, 1841–1852.

Li, H., and Durbin, R. (2010). Fast and accurate long-read alignment with Burrows-Wheeler transform. Bioinformatics *26*, 589–595.

Li, H., Handsaker, B., Wysoker, A., Fennell, T., Ruan, J., Homer, N., Marth, G., Abecasis, G., and Durbin, R.; 1000 Genome Project Data Processing Subgroup (2009). The Sequence Alignment/Map format and SAMtools. Bioinformatics *25*, 2078–2079.

Li, Y., Schwab, C., Ryan, S.L., Papaemmanuil, E., Robinson, H.M., Jacobs, P., Moorman, A.V., Dyer, S., Borrow, J., Griffiths, M., et al. (2014). Constitutional and somatic rearrangement of chromosome 21 in acute lymphoblastic leukaemia. Nature *508*, 98–102.

Lin, T.T., Letsolo, B.T., Jones, R.E., Rowson, J., Pratt, G., Hewamana, S., Fegan, C., Pepper, C., and Baird, D.M. (2010). Telomere dysfunction and fusion during the progression of chronic lymphocytic leukemia: evidence for a telomere crisis. Blood *116*, 1899–1907.

Lin, T.T., Norris, K., Heppel, N.H., Pratt, G., Allan, J.M., Allsup, D.J., Bailey, J., Cawkwell, L., Hills, R., Grimstead, J.W., et al. (2014). Telomere dysfunction accurately predicts clinical outcome in chronic lymphocytic leukaemia, even in patients with early stage disease. Br. J. Haematol. *167*, 214–223.

Lopez, V., Barinova, N., Onishi, M., Pobiega, S., Pringle, J.R., Dubrana, K., and Marcand, S. (2015). Cytokinesis breaks dicentric chromosomes preferentially at pericentromeric regions and telomere fusions. Genes Dev. *29*, 322–336.

Mardin, B.R., Drainas, A.P., Waszak, S.M., Weischenfeldt, J., Isokane, M., Stütz, A.M., Raeder, B., Efthymiopoulos, T., Buccitelli, C., Segura-Wang, M., et al. (2015). A cell-based model system links chromothripsis with hyperploidy. Mol. Syst. Biol. *11*, 828.

McClintock, B. (1938). The Production of Homozygous Deficient Tissues with Mutant Characteristics by Means of the Aberrant Mitotic Behavior of Ring-Shaped Chromosomes. Genetics *23*, 315–376.

McClintock, B. (1941). The stability of broken ends of chromosomes in Zea mays. Genetics *26*, 234–282.

Mehine, M., Kaasinen, E., Mäkinen, N., Katainen, R., Kämpjärvi, K., Pitkänen, E., Heinonen, H.R., Bützow, R., Kilpivaara, O., Kuosmanen, A., et al. (2013). Characterization of uterine leiomyomas by whole-genome sequencing. N. Engl. J. Med. *369*, 43–53.

Nik-Zainal, S., Alexandrov, L.B., Wedge, D.C., Van Loo, P., Greenman, C.D., Raine, K., Jones, D., Hinton, J., Marshall, J., Stebbings, L.A., et al.; Breast Cancer Working Group of the International Cancer Genome Consortium (2012a). Mutational processes molding the genomes of 21 breast cancers. Cell *149*, 979–993.

Nik-Zainal, S., Van Loo, P., Wedge, D.C., Alexandrov, L.B., Greenman, C.D., Lau, K.W., Raine, K., Jones, D., Marshall, J., Ramakrishna, M., et al.; Breast Cancer Working Group of the International Cancer Genome Consortium (2012b). The life history of 21 breast cancers. Cell *149*, 994–1007.

Nones, K., Waddell, N., Wayte, N., Patch, A.M., Bailey, P., Newell, F., Holmes, O., Fink, J.L., Quinn, M.C., Tang, Y.H., et al. (2014). Genomic catastrophes frequently arise in esophageal adenocarcinoma and drive tumorigenesis. Nat. Commun. *5*, 5224.

Preibisch, S., Saalfeld, S., and Tomancak, P. (2009). Globally optimal stitching of tiled 3D microscopic image acquisitions. Bioinformatics *25*, 1463–1465.

Quinlan, A.R. (2014). BEDTools: The Swiss-Army Tool for Genome Feature Analysis. Curr. Protoc. Bioinformatics *47*, 1–34.

Rausch, T., Jones, D.T., Zapatka, M., Stütz, A.M., Zichner, T., Weischenfeldt, J., Jäger, N., Remke, M., Shih, D., Northcott, P.A., et al. (2012). Genome sequencing of pediatric medulloblastoma links catastrophic DNA rearrangements with TP53 mutations. Cell *148*, 59–71.

Reijns, M.A., Rabe, B., Rigby, R.E., Mill, P., Astell, K.R., Lettice, L.A., Boyle, S., Leitch, A., Keighren, M., Kilanowski, F., et al. (2012). Enzymatic removal of ribonucleotides from DNA is essential for mammalian genome integrity and development. Cell *149*, 1008–1022.

Rice, G.I., Rodero, M.P., and Crow, Y.J. (2015). Human disease phenotypes associated with mutations in TREX1. J. Clin. Immunol. *35*, 235–243.

Roberts, S.A., and Gordenin, D.A. (2014). Hypermutation in human cancer genomes: footprints and mechanisms. Nat. Rev. Cancer *14*, 786–800.

Roberts, S.A., Sterling, J., Thompson, C., Harris, S., Mav, D., Shah, R., Klimczak, L.J., Kryukov, G.V., Malc, E., Mieczkowski, P.A., et al. (2012). Clustered mutations in yeast and in human cancers can arise from damaged long single-strand DNA regions. Mol. Cell *46*, 424–435.

Roberts, S.A., Lawrence, M.S., Klimczak, L.J., Grimm, S.A., Fargo, D., Stojanov, P., Kiezun, A., Kryukov, G.V., Carter, S.L., Saksena, G., et al. (2013). An APOBEC cytidine deaminase mutagenesis pattern is widespread in human cancers. Nat. Genet. *45*, 970–976.

Roger, L., Jones, R.E., Heppel, N.H., Williams, G.T., Sampson, J.R., and Baird, D.M. (2013). Extensive telomere erosion in the initiation of colorectal adenomas and its association with chromosomal instability. J. Natl. Cancer Inst. *105*, 1202–1211.

Santaguida, S., Tighe, A., D'Alise, A.M., Taylor, S.S., and Musacchio, A. (2010). Dissecting the role of MPS1 in chromosome biorientation and the spindle checkpoint through the small molecule inhibitor reversine. J. Cell Biol. *190*, 73–87.

Scheel, C., and Weinberg, R.A. (2012). Cancer stem cells and epithelial-mesenchymal transition: concepts and molecular links. Semin. Cancer Biol. *22*, 396–403.

Simpson, K., Jones, R.E., Grimstead, J.W., Hills, R., Pepper, C., and Baird, D.M. (2015). Telomere fusion threshold identifies a poor prognostic subset of breast cancer patients. Mol. Oncol. *9*, 1186–1193.

Stephens, P.J., Greenman, C.D., Fu, B., Yang, F., Bignell, G.R., Mudie, L.J., Pleasance, E.D., Lau, K.W., Beare, D., Stebbings, L.A., et al. (2011). Massive genomic rearrangement acquired in a single catastrophic event during cancer development. Cell *144*, 27–40.

Stimpson, K.M., Matheny, J.E., and Sullivan, B.A. (2012). Dicentric chromosomes: unique models to study centromere function and inactivation. Chromosome Res. *20*, 595–605.

Straight, A.F., Cheung, A., Limouze, J., Chen, I., Westwood, N.J., Sellers, J.R., and Mitchison, T.J. (2003). Dissecting temporal and spatial control of cytokinesis with a myosin II Inhibitor. Science *299*, 1743–1747.

Takai, K.K., Kibe, T., Donigian, J.R., Frescas, D., and de Lange, T. (2011). Telomere protection by TPP1/POT1 requires tethering to TIN2. Mol. Cell *44*, 647–659.

Takai, H., Smogorzewska, A., and de Lange, T. (2003). DNA damage foci at dysfunctional telomeres. Curr. Biol. *13*, 1549–1556.

van Mameren, J., Gross, P., Farge, G., Hooijman, P., Modesti, M., Falkenberg, M., Wuite, G.J., and Peterman, E.J. (2009). Unraveling the structure of DNA during overstretching by using multicolor, single-molecule fluorescence imaging. Proc. Natl. Acad. Sci. USA *106*, 18231–18236.

van Steensel, B., Smogorzewska, A., and de Lange, T. (1998). TRF2 protects human telomeres from end-to-end fusions. Cell *92*, 401–413.

Vargas, J.D., Hatch, E.M., Anderson, D.J., and Hetzer, M.W. (2012). Transient nuclear envelope rupturing during interphase in human cancer cells. Nucleus *3*, 88–100.

Waclaw, B., Bozic, I., Pittman, M.E., Hruban, R.H., Vogelstein, B., and Nowak, M.A. (2015). A spatial model predicts that dispersal and cell turnover limit intratumour heterogeneity. Nature *525*, 261–264.

Waddell, N., Pajic, M., Patch, A.M., Chang, D.K., Kassahn, K.S., Bailey, P., Johns, A.L., Miller, D., Nones, K., Quek, K., et al.; Australian Pancreatic Cancer Genome Initiative (2015). Whole genomes redefine the mutational landscape of pancreatic cancer. Nature *518*, 495–501.

Zacharias, D.A., Violin, J.D., Newton, A.C., and Tsien, R.Y. (2002). Partitioning of lipid-modified monomeric GFPs into membrane microdomains of live cells. Science *296*, 913–916.

Zhang, C.Z., Spektor, A., Cornils, H., Francis, J.M., Jackson, E.K., Liu, S., Meyerson, M., and Pellman, D. (2015). Chromothripsis from DNA damage in micronuclei. Nature *522*, 179–184.

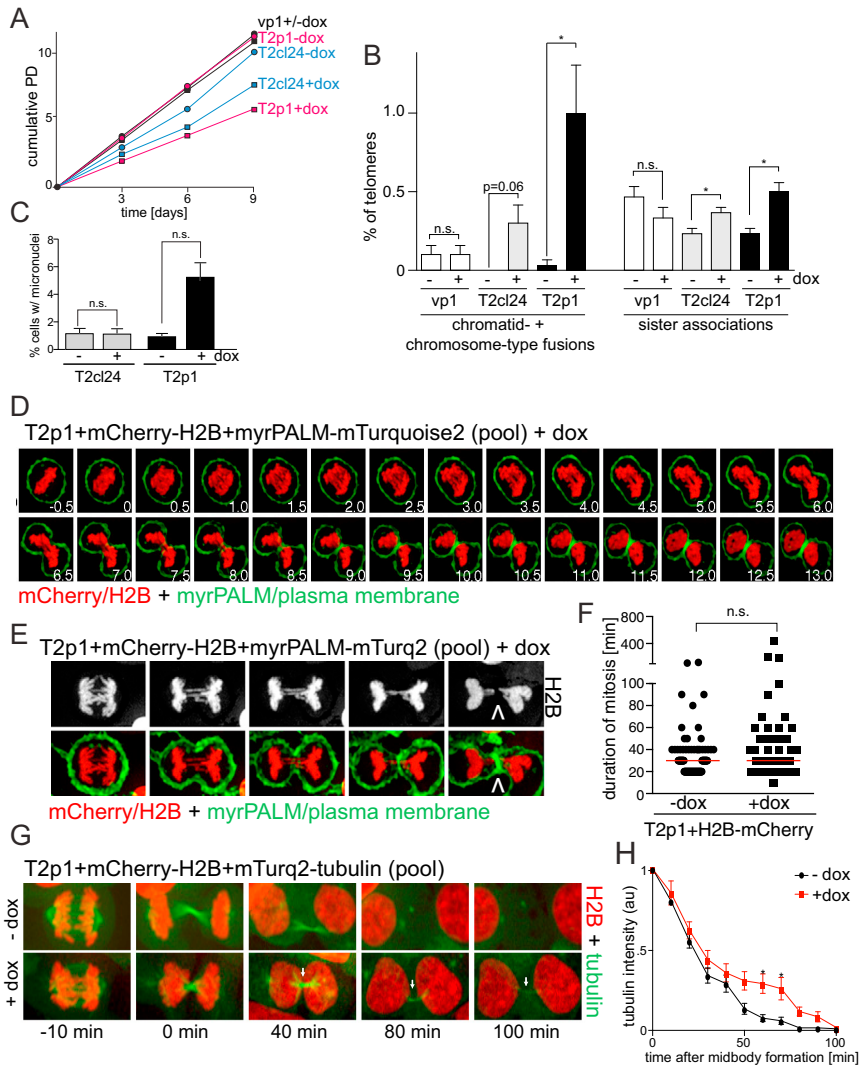

Figure S1. Proliferation, DNA Damage, Micronuclei, and Mitosis after Induction of Telomere Dysfunction, Related to Figure 1

(A) Proliferation of the indicated cell lines before and after induction of telomere fusions with doxycycline.

(B) Quantification of telomere fusions as determined in Figure 1D in the indicated cell lines at 48 hr after addition of dox. Fusions were classified as chromatid- or chromosome-type (left side of graph). Sister chromatid associations were assigned a different classification and scored separately (right side of graph). > 5600 telomeres were examined for each line in each experiment. Data are from 3 independent experiments. Means and SDs are shown. *p $\leq$ 0.05, determined with Student's t test.

(C) Telomere damage does not induce a significant level of micronuclei. Micronuclei were scored using DAPI on the indicated cell lines. > 500 cells were examined at 72 hr after dox-induction of telomere fusions. Data are from 3 independent experiments. Means and SDs are shown. P values were found to be > 0.1 based on Student's t test.

(D) and (E) Examples of myrPALM-mTurquoise2 imaging of cleavage furrow ingression in a cell with anaphase bridges. Arrows in (E) show lack of H2B signals at the cleavage furrow. Stills were captured from movies as in Movie S1, panel 2. Time in (D) is in minutes.

(F) Dox induction of telomere fusions does not significantly delay progression through mitosis. Duration of mitosis was measured using live-cell imaging on individual cells using H2B-mCherry marked cells. Nuclear envelope breakdown and anaphase were used to mark the beginning and end of mitosis, respectively. The red line indicates the median. Datasets were compared by the Mann-Whitney test.

(G) Imaging of tubulin in cells with and without telomere fusions. Stills were captured from movies as in Movie S1, panel 3. Arrows point to persistent tubulin signal on the bridge.

(H) Quantification of the mTurquoise-tubulin intensity on the midbody region in cells with (+dox) and without (-dox) telomere fusions. Data were obtained from images as in (G) using 12 cells per condition. Asterisks indicate a significant difference (based on Student's t test) in tubulin intensity at two later time points. There is no significant difference at the other time points. Error bars, SEMs.

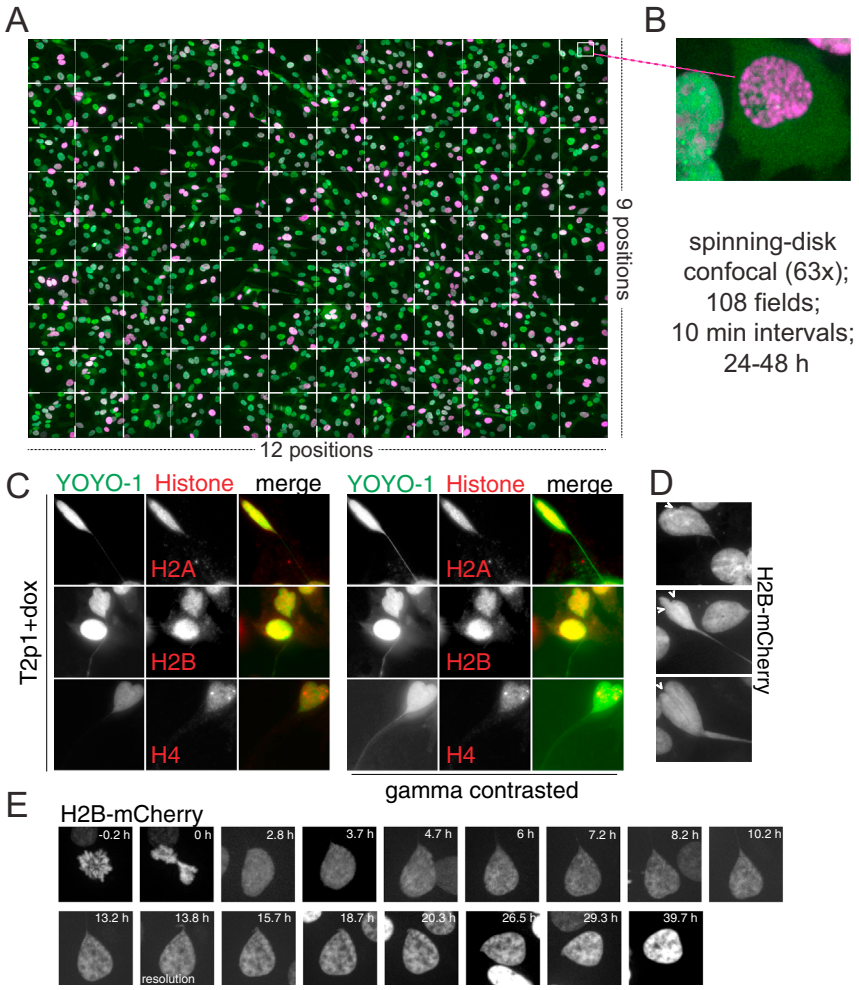

Figure S2. Stitching Microscopy, Reduced Signal for Histones on Chromatin Bridges, and Morphology of Nuclei with Chromatin Bridges, Related to Figure 2

(A) Stitching microscopy used to obtain all movies presented in this study. Images obtained at 63x with spinning-disc microscopy at 10 min acquisition intervals on 108 fields were computationally stitched generating 1-2 day movies. Still was captured from movies as in Movie S2.

(B) Enlarged cell illustrating the resolution of the images in the movies.

(C) IF for the indicated histones on chromatin bridges.

(D) Examples of the morphology of three nuclei (Tp21 + dox) with chromatin bridges. Arrowheads point to invaginations possibly suggesting that the chromosome(s) are anchored in the nucleus and are exerting a pulling force on the nuclear periphery.

(E) Example of the morphological changes of a Tp21 + dox nucleus with a chromatin bridge before and after bridge resolution.

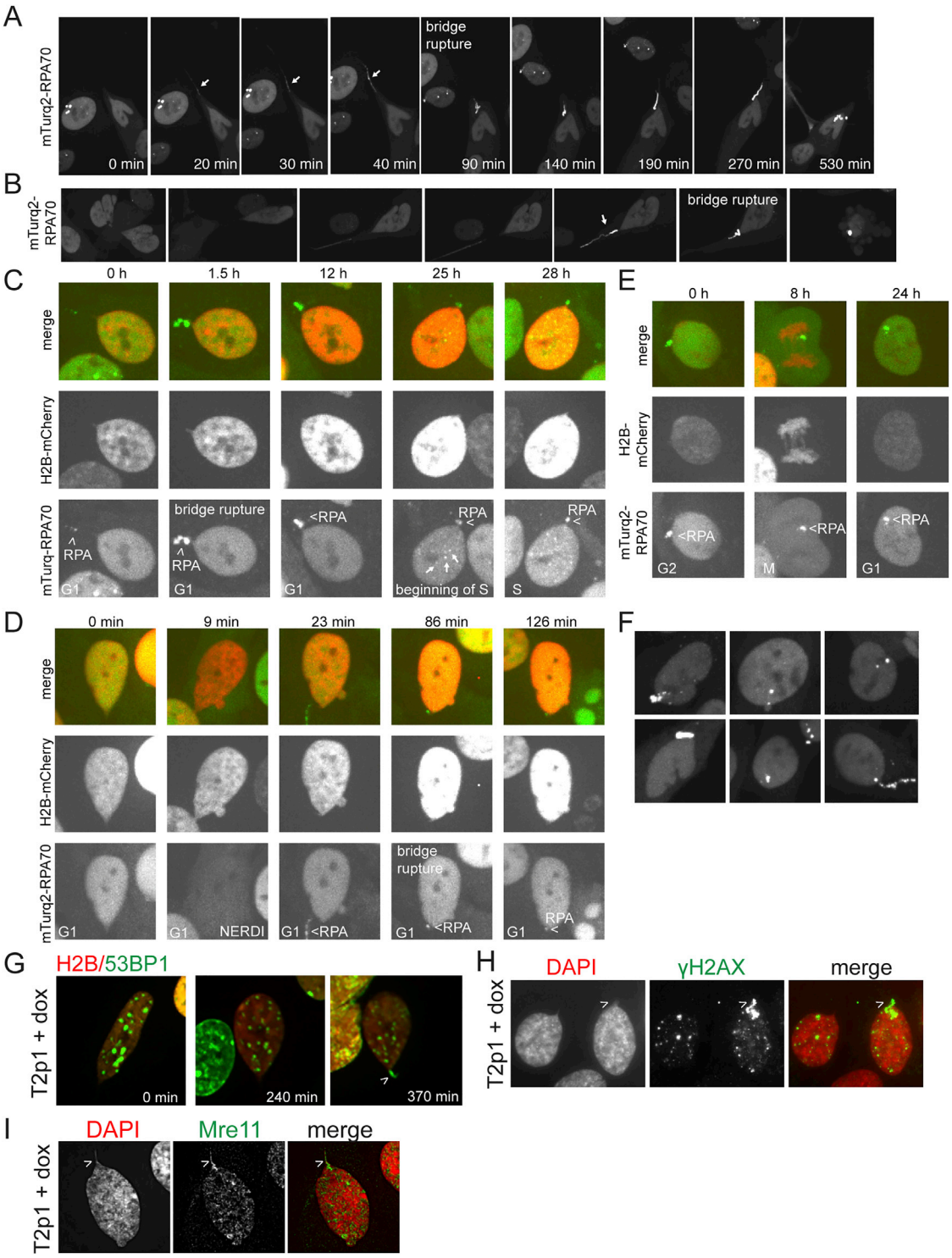

Figure S3. Imaging of mTurquoise2-RPA70 on Chromatin Bridges, Related to Figure 2 and Figure 3

(A–D) Examples of changes in RPA accumulation on chromatin bridges in T2p1+H2B-mCherry+mTurq2-RPA70 cells treated with dox. Bridge resolution, time points, cell cycle stages, and sites of RPA accumulation are highlighted. Arrows in (A) and (B) highlight RPA on chromatin bridges before resolution. Note that the diffuse RPA pattern of the primary nuclei at the time of bridge resolution indicates that the cells have not entered S phase. The punctate RPA pattern indicative of S phase (see arrows in 25 hr image) is shown in (C).

(E) Example of an RPA-coated bridge remnant persisting until the 2nd mitosis and joining a daughter nucleus after cell division.

(F) Examples of RPA-coated bridge remnants in six cells captured post bridge resolution.

(legend continued on next page)

(G) Example of 53BP1 accumulation on chromatin bridges after resolution in T2p1+H2B-mCherry+mTurq2-BP1-2 cells treated with dox.
(H) Example of γH2AX accumulation on chromatin bridges after resolution in T2p1cells treated with dox.
(I) Example of Mre11 accumulation on chromatin bridges after resolution in T2p1cells treated with dox. Images in (G-I) link DNA fragmentation and chromatin bridge resolution.

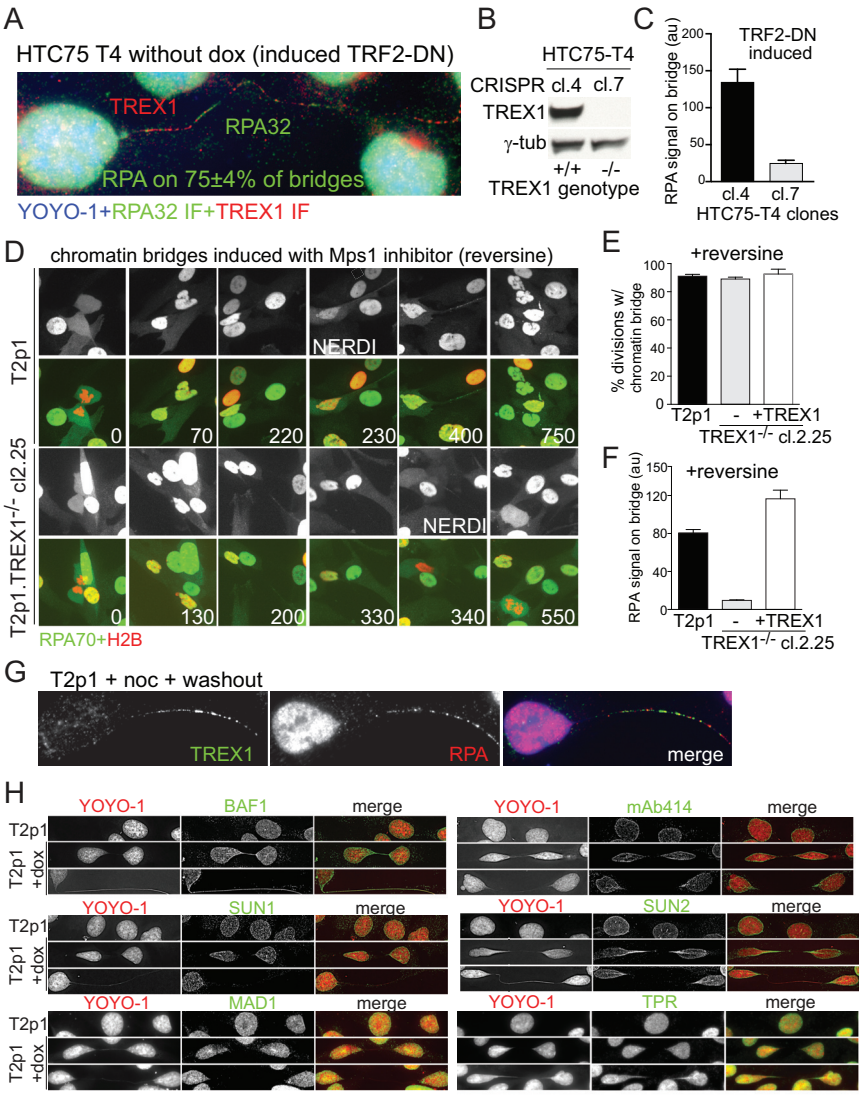

Figure S4. Chromatin Bridges Induced in Different Cell Types and by Different Mechanisms Display the Same Basic Aspects of Chromatin Bridge Biology, Related to Figure 2, Figure 3, and Figure 4

(A) IF for TREX1 and RPA on HTC75 T4 cells with (-dox) induction of telomere fusions. IF signals were merged with DAPI (blue). Approximately 75% of chromatin bridges in HTC75 T4 cells accumulate RPA before resolution in live-cell imaging experiments. Data are derived from > 50 chromatin bridges in 2 independent experiments.

(B) Immunoblot for TREX1 showing absence of TREX1 in a CRISPR/Cas9 edited clone.

(C) Quantification of live-cell imaging experiment showing a reduction of RPA signal on chromatin bridges in TREX1 KO HTC75 T4 cells. > 50 chromatin bridges were examined for each line in each experiment. Data are from 2 independent experiments. Means and SEMs are shown.

(D) Accumulation of RPA on chromatin bridges induced by Mps1 inhibition with reversine. Top panel: T2p1+H2B-mCherry+mTurquoise2-RPA70 cells were treated with reversine immediately before examination by live-cell imaging. Stills showing a NERDI event and mTurquoise2-RPA70 signal on the bridge are shown. Bottom panel: Chromatin bridges induced by Mps1 inhibition in TREX1 KO cells do not accumulate RPA.

(E) Quantification of chromatin bridge formation in cells treated as in (D). > 100 cell divisions were examined for each cell line. Error bars, SEMs.

(F) Quantification of live-cell imaging experiment showing a reduction of RPA signal on chromatin bridges in TREX1 KO T2p1 cells. > 50 chromatin bridges were examined for each line in each experiment. Data are from 2 independent experiments. Means and SEMs are shown.

(G) IF for TREX1 and RPA32 on T2p1 cells after induction of chromatin bridges by nocodazole washout. IF signals were merged with DAPI (blue). Image shows TREX1 and RPA32 localization to chromatin bridge created by nocodazole washout.

(H) BAF1, mAb414, SUN1, SUN2, Mad1, Tpr (green) on T2p1 before and 48 hr after induction of chromatin bridges with dox. DNA was stained with YOYO-1 (red). Images show accumulation of BAF1 on longer chromatin bridges and absence of mAb414, SUN1, SUN2, Mad1, and Tpr signals on chromatin bridges.

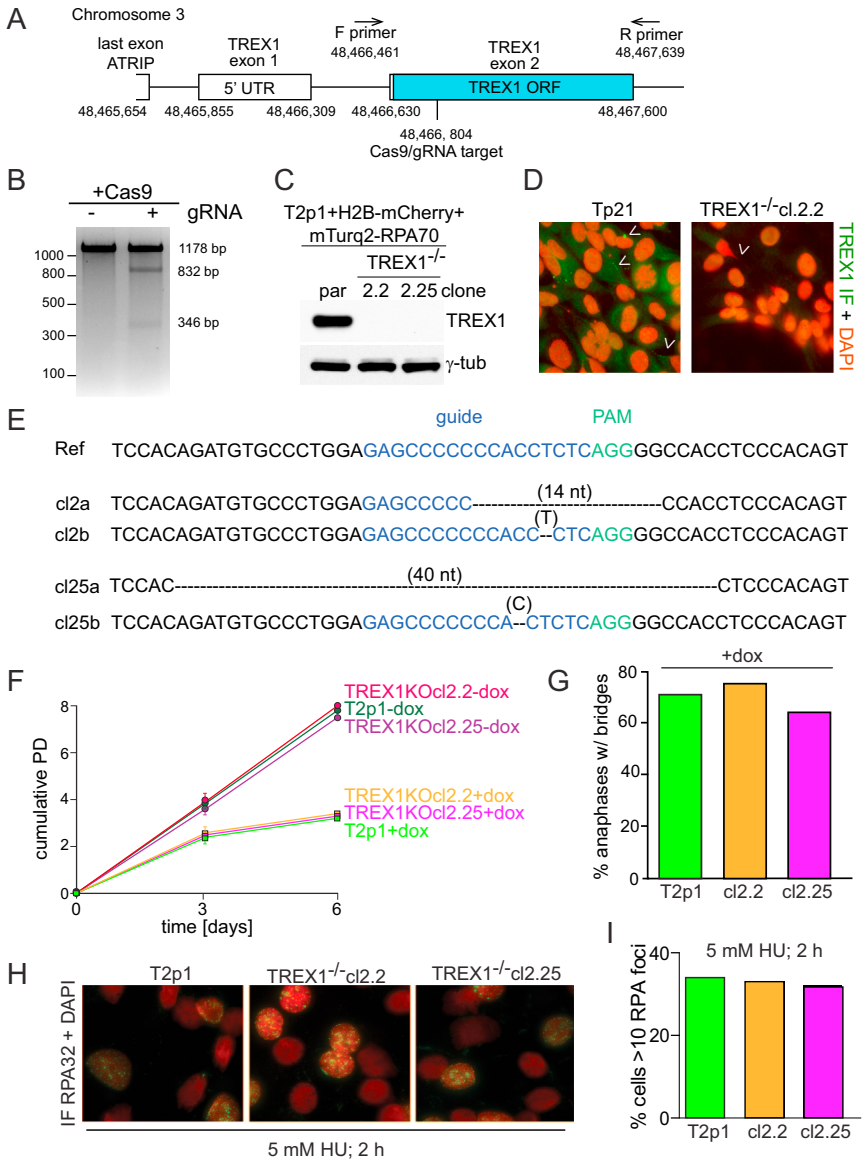

Figure S5. CRISPR/Cas9 Gene Editing of TREX1 and Its Effects on Cell Growth, Induction of Anaphase Bridges and RPA Accumulation at Sites of Replication Stress, Related to Figure 4

(A) Schematic of the TREX1 locus showing landmarks relevant to CRISPR editing.

(B) Surveyor assay showing efficacy of the gRNA targeting TREX1.

(C) Immunoblot for TREX1 showing absence of TREX1 in two CRISPR/Cas9 edited clones.

(D) IF showing absence of TREX1 signal in one of the CRISPR/Cas9 clones. The absence of the signal demonstrates the specificity of the antibody used. Arrowheads point to chromatin bridges and one bridge remnant (left image).

(E) DNA sequence of the two edited TREX1 alleles in the two CRISPR KO clones. Guide RNA region and the PAM are indicated in the reference sequence and the deletions are highlighted in each edited allele. Sequence was derived from TOPO-cloned PCR products obtained with the primers shown in (A).

(F) Proliferation of the TREX1 CRISPR KO clones with and without doxycycline induction of telomere fusions.

(G) Similar levels of anaphase bridges in the parental line and the TREX1 KO clones.

(H) IF for RPA32 on the indicated cells after treatment with HU to induce replication stress.

(I) Quantification of the RPA foci as detected in (H).

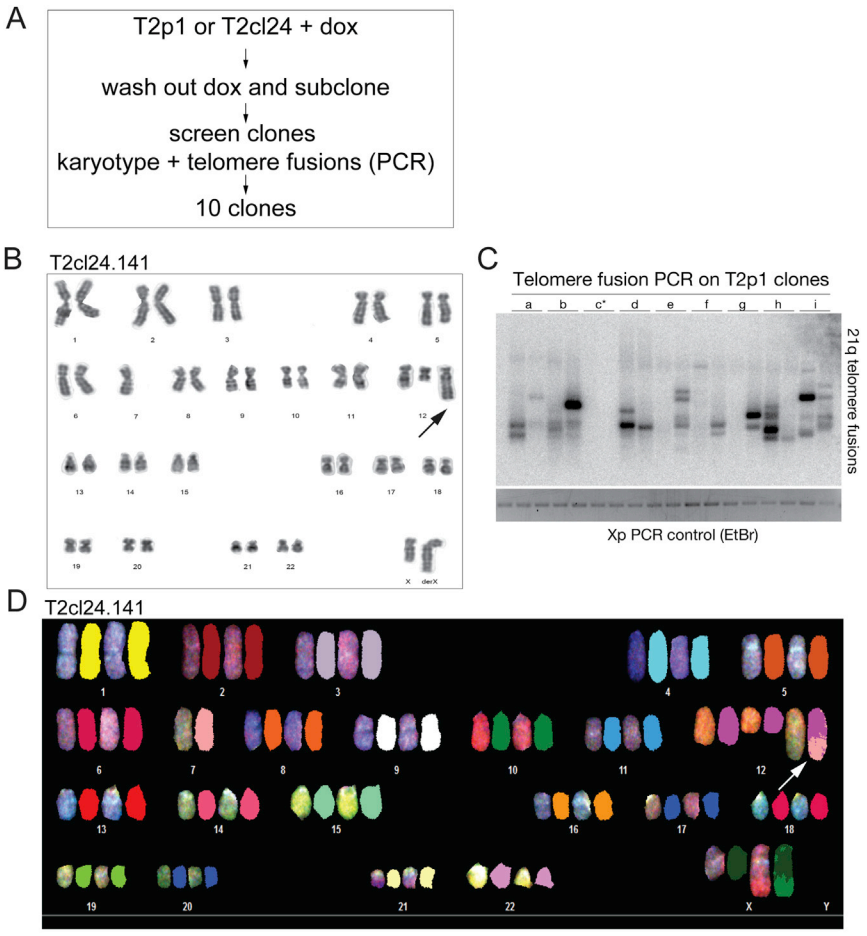

E

cell line	karyo typed	marker positive	fusion PCR positive	sequenced	chromo-thripsis	rearrangements validated by PCR	kataegis validated by Sanger sequencing
T2cl24	39	2/39	4/6	3	1	10/14	1
T2p1 (exp1)	25	5/25	16/23	1	0	NA	NA
T2p1 (exp2)	28	7/28	9/24	7	4	73/118	1

Figure S6. Derivation of Post-telomere Crisis Clones Used for Genomic Sequence Analysis, Related to Figure 5 and Figure 6

(A) Schematic of the steps used to select post telomere crisis clones for sequence analysis.

(B) Example of karyotypic analysis (Tcl24.141) showing a marker chromosome.

(C) Example of telomere fusion PCR on a subset of analyzed clones. Asterisk at clone c: no detectable telomere fusions.

(D) SKY analysis of the clone shown in (B) showing the marker chromosome.

(E) Summary of results from karyotypic analysis (DAPI stain), telomere fusion PCR, whole-genome sequencing, and PCR and Sanger sequencing confirmation of identified rearrangements and kataegis events.

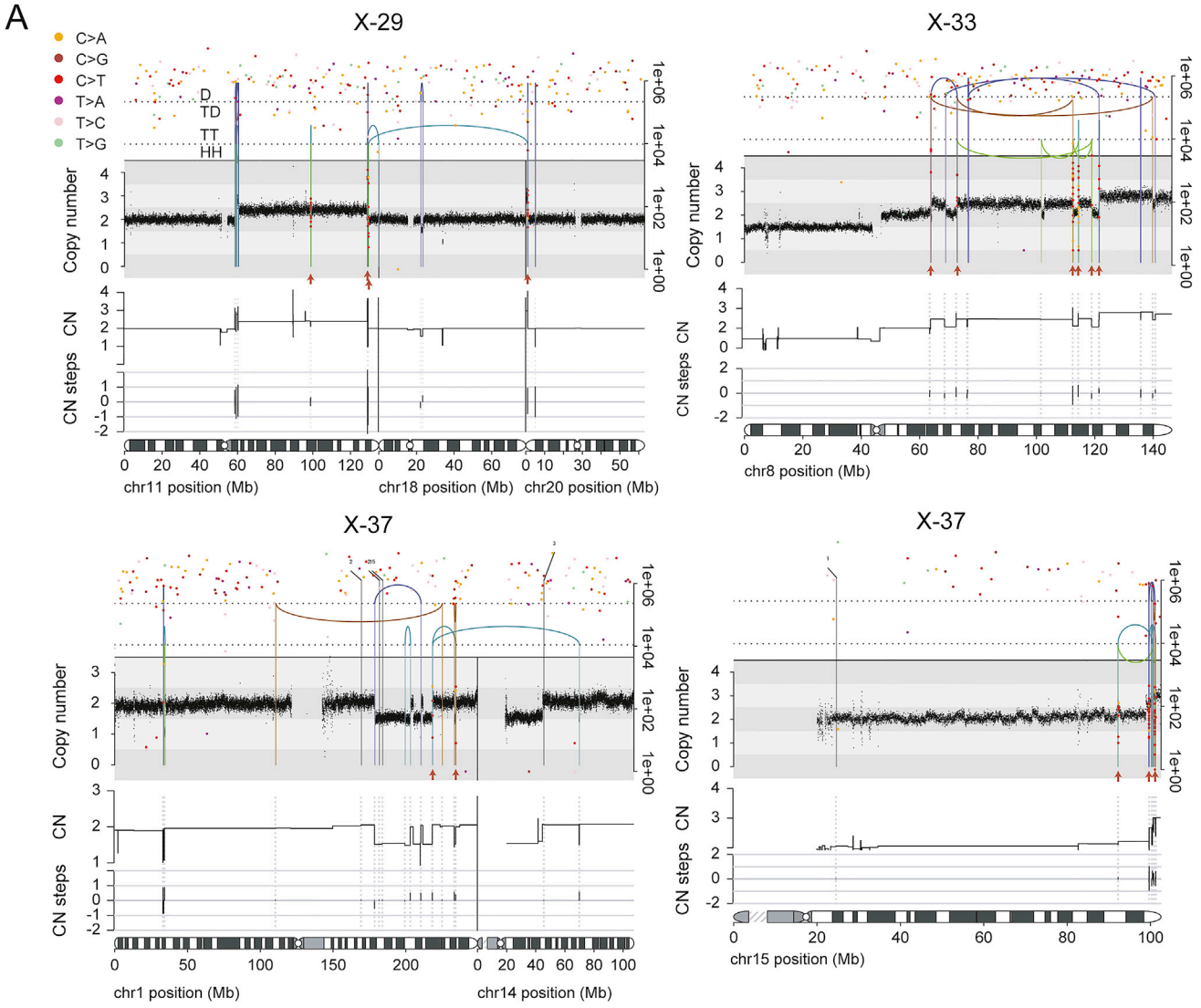

(legend on next page)

Figure S7. Chromothripsis and Kataegis in Post-crisis Clones X-29, X-33, and X-37, and Copy-Number Jump Sizes across Rearrangements, Related to Figure 5

(A) Chromothripsis and rainfall plot of sample X-29 chromosomes 11, 18 and 20, X-33 chromosome 8, X-37 chromosomes 1 and 14, and X-37 chromosome 15. The arcs on the top represent the two ends of rearrangements. The arcs are grouped by the orientations of the two rearrangement ends, with deletion-type (D; +-) rearrangements on top, followed by tandem duplication-type (TD; -+), tail-tail (TT; ++) and head-head (HH;–) type rearrangements. Estimated copy number over genomic windows is shown in the middle. Inferred copy-number segments are shown below the copy number and the bottom section of the graphs show the amount of copy-number change between copy-number segments. The variant allele frequency (VAF) track is shown below the copy-number track. Inferred copy-number segments are shown below VAF and the bottom section of the graphs show the amount of copy-number change between copy-number segments. If chromothripsis took place following a duplicated chromosomal region, the resulting derivative chromosome is expected to involve three copy-number states, but copy-number transitions of only one copy at a time (copy-number steps of +1 or –1). On the other hand if a non-duplicated chromosome underwent chromothripsis and then duplication, there would be expected to be some copy-number steps of +2 or –2.

The positions of point mutations are shown as filled circles. The mutations are colored by mutation type. The y axis value of the mutations indicates the distance of each mutation to the next mutation on the same chromosome, with the respective axis on the right-hand side of the graph. Inferred kataegis clusters are highlighted using red arrows.

(B) Copy-number jumps across rearrangements for all six chromothripsis events across five clones. Every point represents a rearrangement, with the X and Y-axes showing the absolute copy number on the low and high end of the rearrangements, respectively. In chromothripsis events involving three or more copy-number states, a duplication event must have taken place at least either before or after the chromothripsis event. If chromothripsis took place on an unduplicated chromosome and the derivative chromosome was subsequently duplicated, the vast majority of the rearrangements should involve two equal copy-number states and thus the rearrangement jumps should lie on the diagonal. On the other hand if chromothripsis took place on a chromosome with already duplicated parts, rearrangements involving segments of different copy number (off-diagonal points) would be expected.

Cell

Supplemental Information

Chromothripsis and Kataegis Induced by Telomere Crisis

John Maciejowski, Yilong Li, Nazario Bosco, Peter J. Campbell, and Titia de Lange

SUPPLEMENTAL MATERIALS

SUPPLEMENTAL EXPERIMENTAL PROCEDURES

Cell Culture Procedures and Plasmids

RPE1-hTERT cells were obtained from the American Type Culture Collection (ATCC) and cultured in a 1:1 mixture of Dulbecco's Modified Eagle Medium (DMEM) and Ham's F-12 medium (Gibco) (DMEM/F12). HTC75 and Phoenix virus packaging cells were grown in DMEM. Media was supplemented with 10% fetal bovine serum (Gibco), 100 U/ml penicillin/streptomycin (Life Technologies), and 2.5 mM L-glutamine (Life Technologies). Doxycycline was used at 1 μg/ml, blebbistatin (Tocris Bioscience) at 30 μM, monastrol (Tocris Bioscience) at 100 μM, nocodazole (Sigma) at 100 ng/ml, and reversine (Cayman Chemical) at 1 μM. Unless indicated otherwise, analysis was performed 48 h after TRF2-DN transgene induction.

For retroviral transduction, open reading frames were cloned into pQCXIN, pQCXIP, pQCXIB (Clontech) or pQCXIZ, which confer resistance to G418, puromycin, blasticidin, and zeocin, respectively. Constructs were transfected into Phoenix amphotropic packaging cells using calcium phosphate precipitation. Retroviral supernatants were filtered, mixed 1:1 with target cell media and supplemented with 4 μg/ml polybrene. Target cells were infected with retroviral supernatants four times at 12 h intervals. Successfully targeted cells were selected using G418 (0.4 mg/ml), puromycin (5 μg/ml), blasticidin (5 μg/ml), or zeocin (Life Technologies) (400 μg/ml). Clones were isolated by limiting dilution. If transgenes incorporated a fluorescent protein, transduced cells were isolated by FACS. Either pooled cells were analyzed or clones were isolated by subcloning into 96-well plates.

Target sequence for CRISPR/Cas9 mediated gene knockouts was identified by ZiFit (http://zifit.partners.org): sgTREX1-2, 5'-GAGCCCCCCCACCTCTC-(PAM)-3'. Target sequences were incorporated into an AflII-linearized gRNA-cloning vector (Addgene) by Gibson Assembly (New England BioLabs). gRNA plasmids were co-transfected into target cells with an hCas9 expression plasmid (Addgene) by nucleofection (Lonza apparatus). 700,000 cells were mixed with electroporation buffer (freshly mixed 125 mM Na_2HPO_4, 12.5 mM KCl, 55 mM MgCl2 pH 7.75), 5 µg Cas9 plasmid, and 5 µg gRNA plasmid, transferred to an electroporation cuvette (BTX), and electroporated with program T23 for RPE-1 cells or program L005 for HTC75 cells. Cells were then allowed to recover for 48 h before a second round of electroporation. Successful CRISPR/Cas9 editing was confirmed at the polyclonal stage by mutation detection with the SURVEYOR nuclease assay (Transgenomic). Briefly, the region surrounding the predicted Cas9 cut site was PCR amplified (Primer 1: CCTCACCCTCTCCAACTTCC, Primer 2: GCAGCGGGGGTCTTTATTCG), melted, and reannealed. Reannealed PCR products were then incubated with the SURVEYOR nuclease for one hour at 42ºC, and analyzed on a 2% agarose gel with ethidium bromide. Clones were isolated by limiting dilution and screened for TREX1 deletion by Western blotting. Biallelic targeting was verified by sequencing of TOPO-cloned PCR products.

Immunoblotting and immunofluorescence

For immunoblotting, cells were harvested by trypsinization and lysed in 1x Laemmli buffer (50 mM Tris, 10% glycerol, 2% SDS, 0.01% bromophenol blue, 2.5% β-mercaptoethanol) at 10^7 cells/ml. Lysates were denatured at 100ºC and DNA was sheared with a 28 1/2 gauge insulin needle. Lysate equivalent to 10^5 cells was resolved on 8% or 10% SDS/PAGE (Life Technologies) and transferred to nitrocellulose membranes. Membranes were blocked in 5% milk in TBS with 0.1% Tween-20 (TBS-T)

and incubated with primary antibody overnight at 4ºC, washed 3 times in TBS-T, and incubated for 1 h at room temperature with horseradish-peroxidase-conjugated sheep anti-mouse or donkey anti-rabbit secondary antibodies. After three washes in TBS-T, membranes were rinsed in TBS and proteins were developed using enhanced chemiluminescence (Amersham).

For IF, cells were grown on coverslips for 48 h prior to fixation in 2% paraformaldehyde in PBS for 10 min or in ice-cold methanol for 10 min. Coverslips were incubated in blocking buffer (1 mg/ml BSA, 3% goat serum, 0.1% Triton X-100, 1 mM EDTA in PBS) for 30 min, followed by incubation with primary antibodies diluted in blocking buffer for 2 h, washed 3 times with PBS with 0.1% Triton, incubated with secondary antibodies diluted in blocking buffer, and finally DNA was stained with either DAPI or YOYO-1 Iodide (Life Technologies). Coverslips were then mounted in ProLong Gold Antifade Mountant (Life Technologies). Digital images were acquired on a Zeiss Axioplan II microscope equipped with a Hamamatsu C4742-95 camera using Volocity software or with an image restoration system (DeltaVision; Applied Precision) equipped with a cooled charge-coupled device camera (CoolSnap QE; Photometrics), a PlanApo 60x 1.40 NA objective (Olympus America, Inc.), and SoftWoRx software.

For EdU labeling, cells were incubated with EdU for 30 minutes prior to PFA fixation. Incorporated EdU was detected using a Click-iT EdU Alexa Fluor 647 imaging kit (Life Technologies).

The following primary antibodies were used: anti-hTRF2 (rabbit polyclonal, de Lange lab, #647) Zhu et al, 2000; anti-γ-tubulin (mouse monoclonal, Abcam, ab11316); anti-myc (mouse monoclonal, MSKCC Hybridoma Core Facility, #9E10); anti-TREX1 (rabbit monoclonal, Abcam, ab185228); anti-Lamin A/C (mouse monoclonal, Santa Cruz, sc-7292); anti-γH2A.X (mouse monoclonal, Millipore, 05-636); anti-53BP1 (rabbit polyclonal, Novus, 100-304A); anti-FLAG (mouse monoclonal, Sigma, F3165); anti-

RPA32 (mouse monoclonal, Abcam, ab2175); anti-Tpr (mouse monoclonal, Santa Cruz, sc-271565); anti-Histone H2A (rabbit polyclonal, Abcam, ab18255), anti-Histone H2B (rabbit polyclonal, Abcam, ab1790); anti-Histone H4 (rabbit polyclonal, Abcam, ab10158); anti-Lamin B1 (rabbit polyclonal, Abcam, ab16048); anti-BAF1 (rabbit monoclonal, Abcam, ab129184); anti-SUN1 (rabbit polyclonal, Abcam, ab74758); anti-SUN2 (rabbit polyclonal, Abcam, ab87036); anti-Mre11 (rabbit polyclonal, Bethyl) ; anti-Mad1 (rabbit polyclonal, Santa Cruz, sc-67338); anti-LAP2 (rabbit polyclonal, Bethyl); anti-mAb414 (mouse monoclonal, Abcam, ab24609).

Live-cell Imaging

Cells were plated onto 35 mm glass bottom dishes (MatTek) 48 h before imaging. One h before imaging cell culture media was replaced with phenol red-free DMEM/F12 medium. Live cell imaging was performed using a CellVoyager CV1000 spinning disk confocal system (Yokogawa, Olympus) equipped with 445, 488, and 561 nm lasers, a Hamamatsu 512 x 512 EMCCD camera. Pinhole size was 50 µm. Images were acquired at the indicated intervals using a UPlanSApo 60x/1.3 silicone oil objective with the correction collar set to 0.17. The pixel size in the image was 0.27 µm. The following emission filters were used for image acquisition: 480/40 or 470/24 for mTurquoise2-tagged proteins, and 617/73 for mCherry-tagged proteins. 17 µm z-stacks were collected at 0.5 µm steps or 16 µm z-stacks were collected at 2.0 µm steps. Temperature was maintained at 37ºC in a temperature-controlled enclosure with CO_2 support. Maximum intensity projection of z-stacks and adjustment of brightness and contrast were performed using Fiji software. Image stitching was done with the Fiji plugin Grid/Collection stitching (Preibisch et al., 2009) with 20% tile overlap, linear blending, a 0.30 regression threshold, a 2.50 max/avg. displacement threshold, and a 3.50 absolute

displacement threshold. Images were cropped and assembled into figures using Photoshop CS5.1 (Adobe).

Telomere fusion PCR

Fusion PCR to detect telomeric fusions was performed essentially as described (Letsolo et al., 2010; Capper et al., 2007). Genomic DNA was extracted using phenol/chloroform, solubilized by digestion with EcoRI, and quantitated by Hoechst 33258 fluorometry (Hoefer). Subtelomeric primers used for amplification of telomeric fusions were XpYpM: ACCAGGTTTTCCAGTGTGTT, 17p6: GGCTGAACTATAGCCTCTGC, 21q4: GGGACATATTTTGGGGTTGC. XpYpc2tr: GCTATGGCTTCTTGGGGC, was included for control amplification of XpYp subtelomeric DNA. PCR conditions were as follows: 50 ng of input genomic DNA, supplemented with Fail Safe PCR buffer H and Fail Safe Enzyme Mix (Epicentre). Cycling conditions were 1 cycle of 95ºC for 15 seconds, followed by 26 cycles of 95ºC for 15 seconds, 58º C for 20 seconds, 68ºC for 10 minutes, and finally 1 cycle of 68ºC for 10 min.

Products were resolved by 0.7% 1x TAE agarose gel electrophoresis, transferred to a Hybond membrane, and detected with a random-primed α-^{32}P-labeled (GE Healthcare) probe specific for the TelBam11 family of subtelomeres (Brown et al., 1990; Riethman et al., 2004). Primers used for TelBam11 probe generation were 21q4 and 21q-seq-rev2: ACACAGAAGGTTGATATACACAG. Control amplification of the XpYp subtelomere was detected with an XpYp subtelomere specific probe generated by PCR with the following primers: XpYpO: CCTGTAACGCTGTTAGGTAC, XpYpG: AATTCCAGACACACTAGGACCCTGA. Hybridized signal was detected by exposing the membrane to a PhosphorImager screen overnight and imaging with a Storm 820 Molecular Imager (Molecular Dynamics).

Analysis of telomere fusions and karyotypes

Cells were incubated with 0.1 μg/ml colcemid (Roche) for 30 min, harvested by trypsinization, resuspended in 0.075 M KCl, incubated at 37ºC for 10 min, and fixed overnight in methanol and acetic acid (3:1) at 4ºC. Fixed cells were dropped onto glass slides and the slides were dried overnight. Cells were rehydrated in PBS for 10 min, dehydrated with 75%, 95%, and 100% ethanol and air dried before hybridization in hybridization solution (70% formamide, 1 mg/ml blocking reagent (Roche), 10 mM Tris-HCl (pH 7.2), TAMRAOO-$(TTAGGG)_3$ PNA probe (Applied Biosystems). Slides were then denatured at 80ºC for 5 min and hybridized for 2 h at room temperature. Slides were washed 2 times for 15 min in wash solution #1 (70% formamide, 10 mM Tris-HCl, (pH 7.2)), and 3 times for 5 min in wash solution #2 (0.1M Tris-HCl (pH 7.2), 0.15M NaCl, 0.08% Tween-20). DNA was stained with DAPI. Slides were mounted in ProLong Gold Antifade Mountant (Life Technologies).

Karyotypic analysis was done on DAPI stained metaphases, G-banded metaphases, or by spectral karyotyping. For spectral karyotyping, cell lines were cultured with colcemid (0.005 μg/mL) at 37°C for 45 minutes, resuspended in 0.075 M KCl, incubated at 37°C for 10 minutes, and then fixed in methanol-acetic acid (3:1). Metaphase spreads from the fixed cell suspension were hybridized with SKY painting probe according to the manufacturer's protocol (Applied Spectral Imaging, Carlsbad, CA). SKY images were acquired with an SD300 Spectracube (Applied Spectral Imaging, Carlsbad, CA) mounted on a Nikon Eclipse E800 microscope using a custom-designed optical filter (SKY-1) (Chroma Technology, Brattleboro, VT). For each cell line, a minimum of 20 metaphases were captured and fully karyotyped. The breakpoints on the SKY-painted chromosomes were determined by comparison with corresponding DAPI karyotype and chromosomal abnormalities described according to the International

System of Human Cytogenetic Nomenclature (ISCN) 2013. CMA-chromosome banding was performed using standard methods.

Image quantitation

Chromatin bridge resolution was determined by manually tracking pairs of daughter cells. Bridge resolution was inferred to take place when the base of the bridge became slack and/or recoiled. The mean fluorescence intensity of mTurquoise2-tubulin at the midbody was measured every 10 minutes using Fiji software. Values were corrected for background and the initial signal intensity of each cell was set to 1. S phase timing was marked by the appearance of stable RPA foci in the primary nucleus.

Dynamics of NERDI events were calculated as described (Hatch et al., 2013). Briefly, the mean fluorescence intensity of NLS-3xmTurquoise2 in a region of interest in the nucleus was measured every 30 seconds over the course of a rupturing event using Fiji software. The peak fluorescence intensity was set to 1, and the lowest fluorescence intensity was set to 0. Rupturing curves were fit to a plateau followed by a one-phase decay curve where the plateau value was set to 1. Recovery curves were fit to one-phase associations. Curve fitting was performed using Prism 6 (GraphPad).

RPA signals on chromatin bridges were quantified by measuring the mean RPA intensity of 10 relevant regions on each chromatin bridge in fixed samples using Fiji software. Background intensity was subtracted and values were averaged within each experiment. Independent experiments were averaged to produce the graph in Figure 4H. Since RPA accumulation on chromatin bridges is usually a late event only bridges greater than 50 μm in length were included in this analysis. For RPA signals quantified in live cell samples (Fig. S4C,F) measurements were taken using Fiji software immediately before bridge rupture or within 16 hours of anaphase.

X-ten sequencing

DNA from the post-crisis samples and parental lines was sequenced on the Illumina X10 platform to a target coverage of 30x whole human genome. Sequencing libraries were synthesized from genomic DNA on robots according to manufacturer's protocols. Cluster generation and sequencing were performed using the manufacturer pipelines. Average sequence coverage achieved across the samples was 33.3x (range, 27.4-35.9x).

Mapping and analysis

Mapping to the human genome was performed using the BWA algorithm (Li and Durbin, 2010), using the BWA mem version 0.7.8. The exact genome build used was hs37d5.

Copy number analysis

The reference genome was divided into windows expected to generate an equivalent number of reads as done previously (Campbell et al., 2008; Li et al., 2009) was used to extract mapped reads with a mapping quality of at least 35 and with the following flags:

- Properly paired
- Non-secondary
- QC-pass
- Non-duplicate
- Non-supplementary

The number of reads overlapping with each genomic window was counted using BEDTools (Quinlan, 2014). Copy number was inferred from read depth data as described previously (Li et al., 2014).

Rearrangement calling and chromothripsis

The sequence data from all sequenced samples was merged. Clusters of abnormally paired read pairs were identified from the merged sequence data using an in-house algorithm 'Brass'. Raw rearrangement calls supported by clusters of abnormally mapped read pairs were called if the clusters were formed of at least four read pairs all from the same sample. An exception was made with X-37, whose rearrangement data was noisier than other samples; for rearrangement calls to be made in X-37 at least six read pairs were required. The raw rearrangements were filtered, as has been described previously (Li et al., 2014). Statistical testing for segment orders was performed using Spearman correlation and for other criteria done as in Li et al., 2014.

Published chromothripsis criteria (Korbel and Campbell, 2013) were used to assess regions with complex clusters of chromothripses. 1. Clustering of breakpoints: Applicable. Five out of nine regions with high density of rearrangements show strong clustering of rearrangement breakpoints. 2. Regularity of oscillating copy-number stages: Applicable. As opposed to "conventional chromothripsis," copy numbers oscillate over multiple copy number states since chromothripsis takes place on chromosomes amplified through BFBs. 3. Interspersed loss and retention of heterozygosity: Applicable. Interspersed loss and retention of heterozygosity was present in multiple chromosomes with chromothripsis. 4. Prevalence of rearrangements affecting a specific haplotype: Applicable. Karyotyping analysis confirms prevalence of rearrangements on a specific haplotype. 5. Randomness of DNA segment order and fragment joins: Applicable. Rearrangements join orientations in chromothripsis regions are consistent with random draws from a uniform multinomial distribution. However, the chromothripsis events involve fairly low numbers of intra-chromosomal rearrangements, which would decrease power in finding statistical departures from a uniform multinomial distribution. 6. Ability to

walk the derivative chromosome: Not applicable, as chromothripsis takes place on chromosomes with preceding duplication through BFBs. In this scenario, it would be impossible to walk the derivative chromosome (Li et al., 2014).

Computation of variant allele frequency

Samtools (v1.2) and bcftools (v1.2) were used to generate a list of variants in the parental clone with default parameters. Of the output variants, only heterozygous biallelic SNPs with the highest variant quality (222) were included, yielding 1,669,777 heterozygous loci in the clone. Samtools and bcftools were then used to compute the variant allele frequency at these reference heterozygous loci.

Mutation calling and kataegis

Point mutations were called using an in-house algorithm 'Caveman' as before (Nik-Zainal et al., 2012a). The RPE-1/Rbsh/p21sh/rtTA clone from which T2p1 and T2cl24 were derived (see Table S1) was used as the reference sample. Raw mutations were filtered as follows:

- Homopolymer filter. Mutations which had a homopolymer repeat of at least six bases on either side of the mutation and where the mutated base was same as the base of the homopolymer repeat(s) were removed.
- Soft-clip filter. Mutations where more than half of the supporting reads were soft-clipped were removed.
- Remapping filter. For each raw mutation, all the mutation-supporting reads were extracted. The reads were mapped, using BWA mem, to a database of 'decoy-sequences', which included all the sequences other than autosomes, chrX, chrY and chrM in GRCh38 and hs38d1. In addition, the HLA region alternative haplotypes were obtained from

http://hgdownload.soe.ucsc.edu/goldenPath/hg19/bigZips/chromFa.tar.gz and added to the decoy sequence database. The remapping difference score was obtained for each read by subtracting the original BWA mem mapping score with the mapping score from remapping the read to the decoy sequence database. Mutations that had an average remapping score over supporting reads < 40 were removed.

Kataegis mutation clusters were detected using visual inspection based on the criteria of short inter-mutation distance (generally <2kb) between cytosine mutations that were processive and enriched with TpC context.

Association of mutation clusters and rearrangements

The distances from the center (middle point between the first and the last mutation) of kataegis events to rearrangement breakpoints were computed manually. To associate a rearrangement breakpoint with a kataegis cluster, the rearrangement breakpoint had to have the right orientation with respect to its relative position to the kataegis cluster. Thus, rearrangements before and after a kataegis cluster in reference genome coordinates were required to be of - and + orientation, respectively.

In some cases a kataegis event was clearly adjacent to a rearrangement breakpoint based on copy number data, but the associated rearrangement call was missed (e.g. X-25 chromosome 13, Figure 5B). In these cases the distance from the kataegis event to the copy number segmentation breakpoint was used instead. Analogous to the rearrangement orientation requirement, copy number segmentation breakpoints before or after a kataegis cluster were required to have a copy number increase or decrease, respectively.

SUPPLEMENTAL TABLE S1. Derivation of cell lines used in this study. Related to Figure 1-4.

Derivation of vp1, T2p1, and T2cl24				
	RPE-1	hTERT/hygro		
	RPE-1	hTERT/hygro	Rbsh+p21sh (GFP/puro)	
	RPE-1	hTERT/hygro	Rbsh+p21sh (GFP/puro)	rtTA (blast)
clone	RPE-1/Rbsh/p21sh/rtTA			
vp1 pool	RPE-1/Rbsh/p21sh/rtTA		dox vector (neo)	
T2p1 pool	RPE-1/Rbsh/p21sh/rtTA		dox mycTRF2-DN(IRESneo)	
T2cl24	RPE-1/Rbsh/p21sh/rtTA		dox mycTRF2-DN(neo)	
RPE-1 derivatives				
RPE-1	NLS-3xmTurquoise2 (FACS, clone)			
vp1 derivatives				
vp1	H2B-mCherry (FACS, pool)			
vp1	NLS-3xmTurquoise2 (FACS, clone)			
T2cl24 derivatives				
T2cl24	H2B-mCherry (FACS, pool)			
T2p1 derivatives				
T2p1	NLS-3xmTurquoise2 (FACS, clone)			
T2p1	H2B-mCherry (FACS, clone)			
T2p1 NLS-3xmTurquoise2 derivatives				
T2p1	mCherry-LaminB1 (FACS, pool)			
T2p1	mCherry-LAP2β (FACS, pool)			
T2p1 H2B-mCherry derivatives				
T2p1	H2B-mCherry (FACS, clone) myrPALM-mTurquoise2 (FACS, pool)			
T2p1	H2B-mCherry (FACS, clone) mTurquoise2-TREX1-D18N (FACS, pool)			
T2p1	H2B-mCherry (FACS, clone) mTurquoise2-RPA70 (FACS, clone)			
T2p1	H2B-mCherry (FACS, clone) mTurquoise2-tubulin (FACS, pool)			
T2p1	H2B-mCherry (FACS, clone) mTurquoise2-BP1-2 (FACS, pool)			
T2p1 H2B-mCherry mTurquoise2-RPA70 derivatives				
T2p1	H2B-mCherry (FACS, clone) mTurquoise2-RPA70 (FACS, clone) 3xFLAG-TREX1 (IRESzeo, pool)			
T2p1	H2B-mCherry (FACS, clone) mTurquoise2-RPA70 (FACS, clone) 3xFLAG-TREX1D18N (IRESzeo, pool)			
CRISPR TREX1 KOs of T2p1 H2B-mCherry mTurquoise2-RPA70 and derivatives				
T2p1	H2B-mCherry (FACS, clone) mTurquoise2-RPA70 (FACS, clone) CRISPR TREX1-/- clone2.2			
T2p1	H2B-mCherry (FACS, clone) mTurquoise2-RPA70 (FACS, clone) CRISPR TREX1-/- clone2.2 3xFLAG-TREX1 (IRESzeo, pool)			
T2p1	H2B-mCherry (FACS, clone) mTurquoise2-RPA70 (FACS, clone) CRISPR TREX1-/- clone2.2 3xFLAG-TREX1D18N (IRESzeo, pool)			
T2p1	H2B-mCherry (FACS, clone) mTurquoise2-RPA70 (FACS, clone) CRISPR TREX1-/- clone2.25			
T2p1	H2B-mCherry (FACS, clone) mTurquoise2-RPA70 (FACS, clone) CRISPR TREX1-/- clone2.25 3xFLAG-TREX1 (IRESzeo, pool)			
T2p1	H2B-mCherry (FACS, clone) mTurquoise2-RPA70 (FACS, clone) CRISPR TREX1-/- clone2.25 3xFLAG-TREX1D18N (IRESzeo, pool)			
T4 derivatives				
T4	van Steensel et al 1998			
T4	H2B-mCherry (FACS, clone) GFP-RPA70 (FACS, clone)			
T4	H2B-mCherry (FACS, clone) GFP-RPA70 (FACS, clone) CRISPR TREX1-/- clone5			

SUPPLEMENTAL TABLE S2. Karyotypes of sequenced cell lines

	Parental lines
	T2p1: 47,X,der(X)t(X;10)(qter;q21),i(12)(p10) RPE-1/Rbsh/p21sh/rTA: 47,X,der(X)t(X;10)(qter;q21),i(12)(p10)
	T2cl24 derivatives:
141	46,X,der(X)t(X;10)(qter;q21),-7,**psu dic(12;7)(q24;q22)**,i(12)(p10) [18]
	47,X,der(X)t(X;10)(qter;q21),+i(12)(p10),r(12)(p13q24)[2]
144	47,X,der(X)t(X;10)(qter;q21),dup(3)(~p21p25),+i(12)(p10)[17]
	47,X,der(X)t(X;10)(qter;q21),dup(3)(~p21p25),+i(12)(p10),der(6)t(3;6)(?q11;p25)[1]
	47,X,der(X)t(X;10)(qter;q21),dup(3)(~p21p25),+i(12)(p10),der(6)t(6;18)(p25;q11)[1]
	47,X,der(X)t(X;10)(qter;q21),dup(3)(~p21p25),r(12)(p13q24),+i(12)(p10)[1]
	T2p1 derivatives:
I.1	52,X,der(X)t(X;10)(qter;q21),+2,+7,+8,+11,+i(12)(p10),+15[14]
	52,X,der(X)t(X;10)(qter;q21),+2,del(3)(p11),+7,+8,+11,+i(12)(p10),+15[1]
	52,X,der(X)t(X;10)(qter;q21),+2,+der(7)t(2;7)(q11;q11),+8,+11,+i(12)(p10),+15[1]
	52,X,der(X)t(X;10)(qter;q21),+2,+7,+8,+11,+i(12)(p10),+del(15)(?q15)[1]
	54,X,der(X)t(X;10)(qter;q21),+2,+7,+8,+11,+i(12)(p10),+15,+17,+20[1]
X.25	48,X,der(X)t(X;10)(qter;q21),**psu dic(4;13)**,i(12)(p10),der(12)t(8;12)
X.29	48,X,der(X)t(X;10)(qter;q21),**der(11)**,i(12)(p10)
X.32	46,X,der(X)t(X;10)(qter;q21),i(12)(p10),-18
X.33	45,der(X)t(X;10)(qter;q21),**der(8)**,i(12)(p10),-18
X.35	47,X,der(X)t(X;10)(qter;q21),der(6),i(12)(p10)
X.36	45,der(X)t(X;10)(qter;q21),-2,-7,-10,i(12)(p10),der(18)
X.37	42~44,X,der(X)t(X;10)(qter;q21),**der(1)t(1;22)(p36;?q13)**,der(1)t(1;15)(q21;?)t(15;17)(?;q21),+i(12)(p10), der(13)t(13;14)(p11;q24),-14,der(15)t(1;15)(?;q24),**der(18)t(18;22)(?q11;?q11),-17,-22**[cp13]
	Bold: chromothriptic clones and their chromothriptic marker chromosomes. [n] indicates the number of cells showing the indicated karyotype. I.1 was kept in doxycycline for two weeks.

SUPPLEMENTAL REFERENCES

Brown, W. R., MacKinnon, P. J., Villasante, A., Spurr, N., Buckle, V. J., and Dobson, M. J. (1990). Structure and polymorphism of human telomere-associated DNA. Cell *63*, 119-132.

Campbell, P. J. et al. (2008). Identification of somatically acquired rearrangements in cancer using genome-wide massively parallel paired-end sequencing. Nat Genet *40*, 722-729.

Capper, R., Britt-Compton, B., Tankimanova, M., Rowson, J., Letsolo, B., Man, S., Haughton, M., and Baird, D. M. (2007). The nature of telomere fusion and a definition of the critical telomere length in human cells. Genes Dev *21*, 2495-2508.

Hatch, E. M., Fischer, A. H., Deerinck, T. J., and Hetzer, M. W. (2013). Catastrophic nuclear envelope collapse in cancer cell micronuclei. Cell *154*, 47-60.

Korbel, J. O., and Campbell, P. J. (2013). Criteria for inference of chromothripsis in cancer genomes. Cell *152*, 1226-1236.

Letsolo, B. T., Rowson, J., and Baird, D. M. (2010). Fusion of short telomeres in human cells is characterized by extensive deletion and microhomology, and can result in complex rearrangements. Nucleic Acids Res *38*, 1841-1852.

Li, H., and Durbin, R. (2010). Fast and accurate long-read alignment with Burrows-Wheeler transform. Bioinformatics *26*, 589-595.

Li, H., Handsaker, B., Wysoker, A., Fennell, T., Ruan, J., Homer, N., Marth, G., Abecasis, G., Durbin, R., and 1000, G. P. D. P. S. (2009). The Sequence Alignment/Map format and SAMtools. Bioinformatics *25*, 2078-2079.

Li, Y. et al. (2014). Constitutional and somatic rearrangement of chromosome 21 in acute lymphoblastic leukaemia. Nature *508*, 98-102.

Nik-Zainal, S. et al. (2012a). Mutational processes molding the genomes of 21 breast cancers. Cell *149*, 979-993.

Preibisch, S., Saalfeld, S., and Tomancak, P. (2009). Globally optimal stitching of tiled 3D microscopic image acquisitions. Bioinformatics *25*, 1463-1465.

Quinlan, A. R. (2014). BEDTools: The Swiss-Army Tool for Genome Feature Analysis. Curr Protoc Bioinformatics *47*, 11.12.1-11.12.34.

Riethman, H., Ambrosini, A., Castaneda, C., Finklestein, J., Hu, X. L., Mudunuri, U., Paul, S., and Wei, J. (2004). Mapping and initial analysis of human subtelomeric sequence assemblies. Genome Res *14*, 18-28.

van Steensel, B., Smogorzewska, A., and de Lange, T. (1998). TRF2 protects human telomeres from end-to-end fusions. Cell *92*, 401-413.

Zhu, X. D., Küster, B., Mann, M., Petrini, J. H., & de Lange, T. (2000). Cell-cycle-regulated association of RAD50/MRE11/NBS1 with TRF2 and human telomeres. Nature Genetics, *25*, 347–352.